

Influenza-trained mucosal-resident alveolar macrophages confer long-term antitumor immunity in the lungs

Received: 12 April 2022

Accepted: 9 January 2023

Published online: 20 February 2023

 Check for updates

Tao Wang^{1,2}, Jinjing Zhang^{1,2}, Yanling Wang^{1,2}, Ying Li^{1,2}, Lu Wang^{1,2}, Yangle Yu^{1,2} & Yushi Yao ^{1,2} 

Respiratory viral infections reprogram pulmonary macrophages with altered anti-infectious functions. However, the potential function of virus-trained macrophages in antitumor immunity in the lung, a preferential target of both primary and metastatic malignancies, is not well understood. Using mouse models of influenza and lung metastatic tumors, we show here that influenza trains respiratory mucosal-resident alveolar macrophages (AMs) to exert long-lasting and tissue-specific antitumor immunity. Trained AMs infiltrate tumor lesions and have enhanced phagocytic and tumor cell cytotoxic functions, which are associated with epigenetic, transcriptional and metabolic resistance to tumor-induced immune suppression. Generation of antitumor trained immunity in AMs is dependent on interferon- γ and natural killer cells. Notably, human AMs with trained immunity traits in non-small cell lung cancer tissue are associated with a favorable immune microenvironment. These data reveal a function for trained resident macrophages in pulmonary mucosal antitumor immune surveillance. Induction of trained immunity in tissue-resident macrophages might thereby be a potential antitumor strategy.

Innate myeloid cells, including macrophages and monocytes, have the potential for enhanced responsiveness to secondary stimulation^{1–7}. Such phenotypes in innate myeloid cells are now collectively termed ‘trained immunity’^{8,9}. Owing to the lack of strict antigen/pathogen specificity of the response, trained innate cells have enhanced immune responses to a variety of heterologous stimulants⁸. Depending on the nature and route of introduction of primary stimulation, trained immunity can develop either systemically in hematopoietic progenitors and circulating monocytes or locally in tissue-specific macrophage populations^{3,10,11}. Although trained macrophages have been widely studied for their anti-infectious functions in both humans and experimental animals, the potential function in antitumor immunity (particularly at specific tissue sites) is less clear^{12–15}.

Tissue-resident macrophages have been shown to be a major source of tumor-associated macrophages (TAMs) in both humans and mice, and resident macrophage-derived TAMs have critical functions in oncogenesis at specific tissue sites, such as the lung, liver and pancreas^{16–19}. As the most abundant leukocyte subset in tumor lesions, TAMs can have protumor functions via a variety of mechanisms, including immunosuppression and angiogenesis²⁰. Alternatively, TAMs can be conditioned for antitumor functions via phagocytosis, presentation of tumor antigens and secretion of antitumor molecular mediators^{21,22}. Therefore, the functional status of resident macrophages via generating resident macrophage-derived TAMs is a deciding factor of tumor development and progress at specific tissue sites. Current macrophage-targeting therapies rely on the short-term effect of

¹Institute of Immunology and Sir Run Run Shaw Hospital, Zhejiang University School of Medicine, Hangzhou, Zhejiang, China. ²Liangzhu Laboratory, Zhejiang University Medical Center, Hangzhou, Zhejiang, China. ✉e-mail: yaoyushi@zju.edu.cn

therapeutics^{23–25}. Little is known about whether long-lasting antitumor reprogramming can be achieved in macrophages, in particular in self-sustaining resident macrophages.

The lungs are a preferential target organ of both primary and metastatic malignancies^{26–28}. Alveolar macrophages (AMs), a subset of lung-resident and self-sustaining macrophages of embryonic ontogeny, have been shown to have critical effects in lung malignancies^{17,18,29}. Meanwhile, the lungs are often exposed to a variety of respiratory pathogens, including viral pathogens such as influenza virus, adenovirus (AdV) and coronavirus^{30,31}. Respiratory viruses typically cause acute infection and have been shown to induce trained immunity in AMs with long-lasting anti-infectious functions^{11,32}. Despite these important findings, the potential role of respiratory viral infection-induced trained AMs in lung malignancies is not well characterized.

Here, we show (in mouse models) that after recovery from influenza A virus (IAV) infection, the lungs are capable of long-lasting antitumor immunity. IAV-exposed resident AMs have cardinal features of trained immunity and have enhanced phagocytic and tumor cytotoxic functions. Together, these findings show that tissue-resident trained macrophages have long-lasting antitumor innate immune functions at specific tissue sites and indicate that modulation of trained immunity in tissue-resident macrophages might be an antitumor strategy with long-term effects.

Results

Acute IAV infection induces long-lasting pulmonary antitumor immunity

To study the long-term effect of acute IAV infection on pulmonary antitumor immunity, wild-type (WT) C57BL/6 mice were infected intranasally (i.n.) with a sublethal dose of IAV. As previously described³³, IAV infection induces respiratory inflammation, characterized by acute leukocyte infiltration, production of proinflammatory cytokines and transient body weight loss, that was resolved by around 2 weeks after infection (Extended Data Fig. 1a–e). At 30 d after infection, mice were injected intravenously (i.v.) with luciferase-expressing B16 melanoma cells (B16-luc) to inoculate tumor cells in the lungs (Fig. 1a). Compared to uninfected mice (PBS), significantly prolonged survival was observed in IAV-infected mice (Fig. 1b). Lung tumor burdens were also found to be lower in IAV-infected mice, as demonstrated by reduced B16-luc-specific gene transcripts of premelanosome (*Pmel*)³⁴ and luciferase in the lung (Extended Data Fig. 2a) and reduced luciferin tumor signals in the lung area (Fig. 1c,d). Consistent with *in vivo* tumor imaging observations, macroscopic evaluation of the lungs at the experimental endpoint showed a drastic reduction of visible B16 tumor nodules in lung lobes in IAV mice compared to that observed in PBS mice (Fig. 1e,f). Lung histopathology also showed lower percentages of lung area occupied by tumor lesions in IAV-infected mice (Fig. 1g,h). In IAV-infected lungs, we observed sporadic consolidation of lung tissues where collagen deposition was evident (Extended Data Fig. 2b). To assess whether reduced lung tumor burden in IAV mice is due to reduced initial tumor

inoculation in the lung, we quantified tumor cells in the lung at 30 min and 24 h after i.v. injection of B16-luc cells expressing green fluorescent protein (GFP)^{27,35}. By quantifying gene transcripts of premelanosome (*Pmel*), dopachrome tautomerase (*Dct*)³⁴ and luciferase as well as the numbers of CD45⁺ GFP⁺ B16 cells, we showed comparable early tumor burdens in the lungs between PBS-treated and IAV-infected mice (Extended Data Fig. 2c,d). These data suggest that the antitumor phenotype in IAV-exposed lungs is not due to reduced initial delivery or inoculation of tumor cells.

Importantly, such an antitumor phenotype was consistently observed when tumor cells were inoculated on days 60 and 120 after IAV infection (Extended Data Fig. 2e–h and Fig. 1i–l), suggesting a long-lasting antitumor immunity induced by acute IAV infection. Moreover, we found that acute AdV infection induced a comparable antitumor phenotype (Extended Data Fig. 2i–l), suggesting that such a virus-induced antitumor immunity is not limited to IAV. IAV-induced antitumor immunity was not observed when tumor cells were subcutaneously (s.c.) inoculated (Extended Data Fig. 2m–p). In a mouse s.c. 4T1 breast cancer model with spontaneous lung metastasis, we further showed that IAV-infected mice had reduced metastatic tumor burdens in the lung compared to uninfected mice, although tumors at primary injection sites were comparable between the two groups of mice (Fig. 1m–o and Extended Data Fig. 2q). To exclude the roles of systemic trained immunity, such as trained granulopoiesis in bone marrow (BM) progenitors with antitumor functions¹⁵, in IAV-induced antitumor protection, we transplanted BM cells from naive or day 30 IAV-infected mice to naive syngeneic hosts (Extended Data Fig. 2r). Host mice were inoculated i.v. with B16 cells after donor BM reconstitution (Extended Data Fig. 2s). There was no difference in B16 tumor burden in the lungs of mice receiving BM from naive versus IAV mice (Extended Data Fig. 2t,u). These data collectively indicate that respiratory viral infections induce antitumor immunity specifically in the lung tissues long after resolution of primary acute anti-infectious immune responses.

Virus-exposed AMs respond to tumors in the lungs

To study whether IAV-induced antitumor immunity is dependent on adaptive T cells, in particular activated T cells with bystander defense activities, we depleted both CD4⁺ and CD8⁺ T cells *in vivo* from day 29 after IAV infection to the experimental endpoint, with B16 cell inoculation on day 30 after infection (Fig. 2a and Extended Data Fig. 3a,b). We found that IAV-induced antitumor immunity in the lung was intact after T cell depletion, as demonstrated by lung macroscopic and histopathological observations (Fig. 2b–e). These data suggest that IAV-induced antitumor immunity in the lung is independent of adaptive T cells.

Macrophages play critical roles in tumor progress, and respiratory viral infection was shown to induce trained immunity in AMs with enhanced responsiveness against heterologous stimulants^{11,17,18}. To directly examine the role of virus-exposed AMs in antitumor immunity, we administered clodronate liposomes intratracheally (i.t.) on

Fig. 1 | Acute IAV infection induces long-lasting pulmonary antitumor immunity.

a, Schema of i.n. IAV infection in mice followed by i.v. inoculation of luciferase-expressing B16-luc melanoma cells. **b**, Survival curve of uninfected (PBS) and IAV-infected mice after tumor inoculation. **c,d**, Luciferin-based *in vivo* tumor imaging (**c**) and average radiance of luciferin signals in the lung area at different days (days 14 to 25) after tumor inoculation in PBS-treated and IAV-infected mice (**d**; the red X in **c** indicates death of the animal). **e,f**, Macroscopic evaluation of the lungs (**e**) and number of macroscopically visible B16 tumor nodules on the surface of lung lobes from PBS- and IAV-infected mice (**f**). **g,h**, Representative lung histopathology images (**g**) and percentage of lung area occupied by tumor lesions based on lung histopathological analysis in mice shown in **e** (**h**). **i,j**, Macroscopic evaluation of the lungs (**i**) and number of macroscopically visible B16 tumor nodules on the surface of lung lobes from PBS- and IAV-infected (IAV₆₁₂₀) mice (**j**).

k,l, Representative lung histopathology images (**k**) and percentage of lung area occupied by tumor lesions based on lung histopathological analysis in mice shown in **i** (**l**). **m**, Schema of IAV infection in BALB/c mice followed by s.c. inoculation of 4T1 breast cancer cells. **n,o**, Representative lung histopathology images (**n**) and percentage of lung area occupied by tumor lesions based on lung histopathological analysis in mice shown in **n** (**o**). Arrows in **n** indicate 4T1 metastatic tumor lesions. Bar graphs are presented as mean \pm s.d. Data are representative of three (**e–h**) or two (**b–d**, **i–l**, **n** and **o**) independent experiments, with the numbers of mice per group indicated ($n = 11$ per group in **b** and **d**; $n = 5$ mice per group in **f** and **h**; $n = 5$ PBS-treated mice and $n = 7$ mice in the IAV₆₁₂₀ group in **j** and **l**; $n = 4$ mice in the PBS group and $n = 6$ mice in the IAV group in **o**). A two-tailed Student's *t*-test was performed for comparisons between two groups. A log-rank (Mantel–Cox) test was used for comparison of survival curves.

day 29 after IAV infection to deplete resident AMs, followed by tumor cell inoculation on day 30 (Fig. 2f and Extended Data Fig. 3c). Additional doses of clodronate liposomes were administered i.v. to deplete

potential monocytic progenitors of AMs (Fig. 2f). Lung macroscopic and histopathological analyses at the experimental endpoint showed that depletion of AMs abrogated the IAV-induced antitumor phenotype

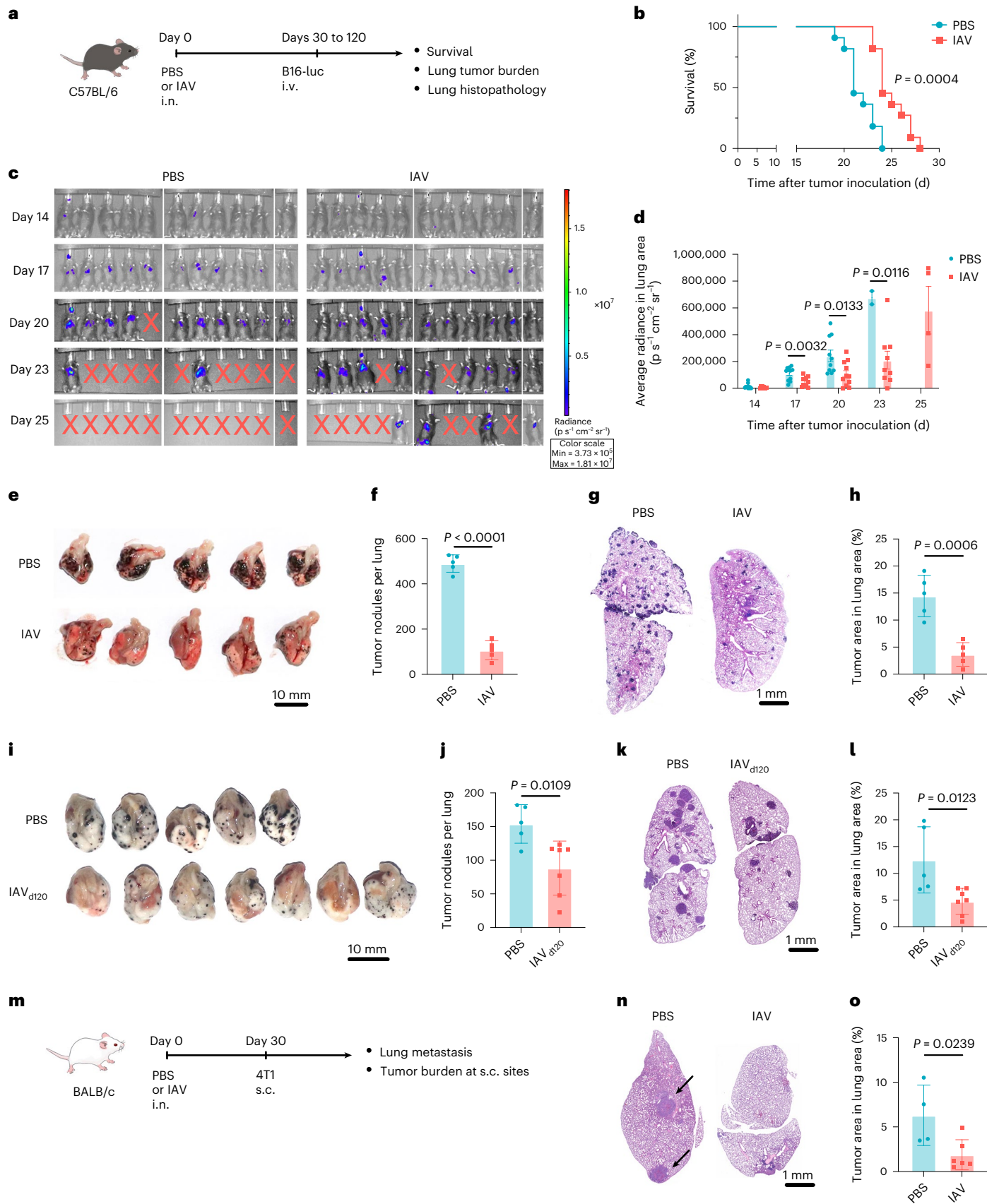


(Fig. 2g–j), suggesting a critical requirement of virus-exposed AMs in mediating antitumor immunity.

To further show the critical role of virus-exposed AMs in antitumor immunity, we isolated AMs from naive or IAV-infected mice on day 30 after infection (Fig. 2k). Isolated AMs were immediately adoptively transferred i.t. into naive syngeneic host mice, followed by inoculation with luciferase-expressing B16-luc cells i.v. (Fig. 2k). On day 17 after tumor inoculation, luciferin-based in vivo tumor imaging showed significantly reduced tumor signals in the lung area of mice receiving IAV-exposed AMs compared to those receiving naive AMs (Fig. 2l,m). Reduced tumor burden in the lungs was also evident in lung macroscopic and histopathological analyses (Fig. 2n–q). Our data thus far indicate that IAV induces long-lasting antitumor innate immunity in the lung, which is mediated by virus-exposed AMs.

IAV infection induces trained immunity in AMs

To characterize AMs from virus-exposed mice, AMs from uninfected or IAV-infected mice were analyzed on day 30 after infection by using a multitude of approaches (Fig. 3a). RNA sequencing (RNA-seq) in purified AMs showed differentially expressed gene transcripts between PBS and IAV AMs, with the transcription of 1,916 genes markedly upregulated and 1,679 downregulated in IAV AMs (Fig. 3b). Moreover, Gene Ontology (GO) enrichment of cluster-specific marker genes revealed upregulation of gene transcripts associated with immune activation and effector functions in IAV AMs (Fig. 3c). In addition to drastic changes in transcriptional profiles, flow cytometry analysis showed that IAV-exposed AMs expressed higher levels of major histocompatibility complex class II (MHC class II) than those from uninfected mice (Fig. 3d). Importantly, IAV-exposed AMs secrete higher amounts of proinflammatory cytokines/chemokines, including tumor necrosis factor (TNF), interleukin-6 (IL-6) and macrophage inflammatory protein 2 (MIP-2), following ex vivo stimulation with lipopolysaccharide (LPS) or live *Streptococcus pneumoniae* that is antigenically irrelevant to IAV (Fig. 3e). By using assay for transposase-accessible chromatin with high throughput sequencing (ATAC-seq) in purified AMs, we showed that chromatin accessibility in 1,725 genes was increased, and chromatin accessibility of 328 genes decreased in IAV versus PBS AMs (Fig. 3f and Extended Data Fig. 4a). GO enrichment of cluster-specific marker genes showed increased chromatin accessibility of genes related to immune activation and effector functions of macrophages in IAV AMs (Fig. 3g). In support of upregulated MHC class II and enhanced potential of proinflammatory mediator production (Fig. 3d,e), ATAC-seq also showed increased chromatin accessibility of genes including MHC class II genes, *Tnf* and *Cxcl2* in IAV AMs (Extended Data Fig. 4b). Gene set enrichment analysis (GSEA) for ATAC-seq signal changes of genes showed enrichment of pathways closely related to trained immunity in AMs, including glycolysis process and the PI3K–Akt, HIF-1 and mTOR signaling pathways (Extended Data Fig. 4c–f). Moreover, IAV AMs showed markedly increased ex vivo oxygen consumption rates (OCRs) and extracellular acidification rates (ECARs) compared to PBS AMs,

indicating prolonged metabolic rewiring (Extended Data Fig. 4g–j). These data collectively suggest that IAV-exposed AMs demonstrate cardinal features of trained immunity.

We next sought to assess whether IAV infection induces protection against heterologous bacterial infection in mice, as we have previously shown in an AdV infection model¹¹. To do this, IAV-infected or uninfected mice were challenged i.t. with a lethal dose of *S. pneumoniae* on day 30 after IAV infection. Compared to IAV-naive mice, IAV-infected mice had improved survival and reduced lung bacterial burdens (Fig. 3h,i). These data indicate that IAV-trained AMs are associated with enhanced antibacterial immunity in the lung, further supporting a trained immunity phenotype in IAV-exposed AMs. To assess whether such an IAV-induced antibacterial trained immunity is contradictory to the well-recognized roles of IAV in bacterial superinfection, we also challenged mice with *S. pneumoniae* i.t. on day 7 after IAV infection (Extended Data Fig. 5a). At this time point, IAV-infected mice showed increased body weight loss and illness scores and succumbed to bacterial superinfection compared to IAV-naive mice (Extended Data Fig. 5b–d). These data suggest that acute-phase IAV infection is associated with bacterial superinfection, while in the immune memory phase after IAV infection, trained AMs exert enhanced antibacterial functions. Our data thus far collectively suggest that IAV infection induces trained immunity in AMs with long-lasting antitumor functions.

IAV-trained AMs develop independently of circulating monocytes

Previous studies suggest that trained AMs are generated either from embryonic-derived resident AMs or from circulating monocytic precursors that reconstitute the lung tissues during inflammation^{11,32,36}. To study the cellular ontogeny of IAV-trained AMs, we compared the expression of characteristic cell surface markers, including CD11b, Ly6C, CD64, CD11c and Siglec-F, in IAV AMs to those in circulating monocytes and embryonic-derived AMs from naive (PBS) mice (Fig. 4a). IAV AMs expressed these selected markers at levels similar to those observed in PBS AMs but with drastic differences observed in monocytes (Fig. 4a). We also compared the RNA-seq profiles of embryonic-derived signature genes in PBS versus IAV AMs (Fig. 4b)³⁶. IAV AMs expressed the majority of embryonic-derived signature genes at levels similar to those observed in embryonic-derived PBS AMs (Fig. 4b). These data support the hypothesis that IAV-trained AMs are generated from embryonic-derived resident AMs but not monocytes.

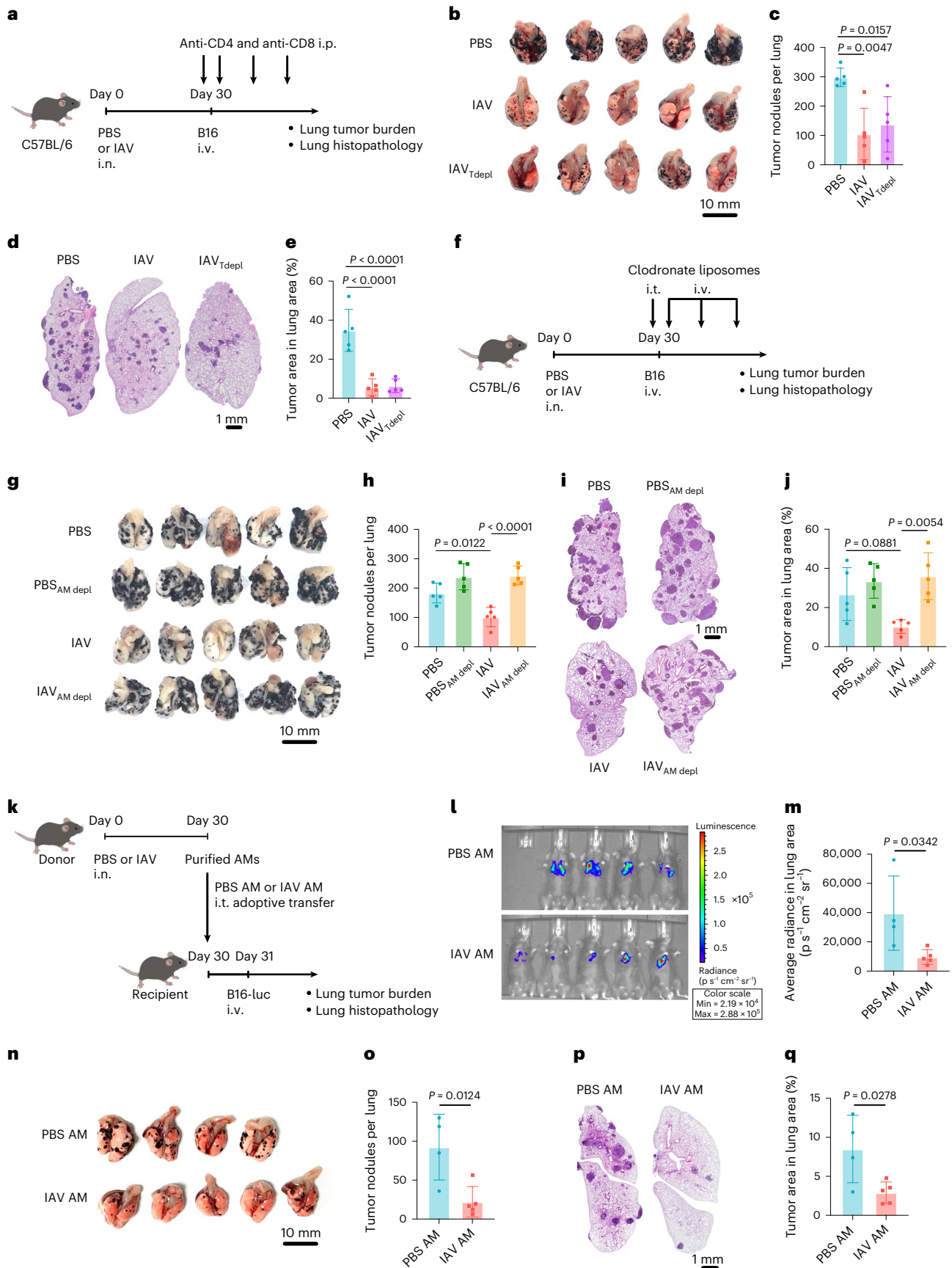
To further show the independence of monocytes in IAV-trained AMs, we administered IAV i.n. to *Ccr2*^{-/-} mice lacking Ly6C^{hi} circulating monocytes, the major contributor of monocyte-derived AMs¹¹. On day 30 after infection, nearly identical numbers of trained AMs with comparable phenotypic and functional changes were observed in *Ccr2*^{-/-} and WT mice (Fig. 4c–e). We also infected parabiotic mice with IAV and examined the levels of chimerism in AMs after infection (Fig. 4f). As expected, chimerism of circulating monocytes

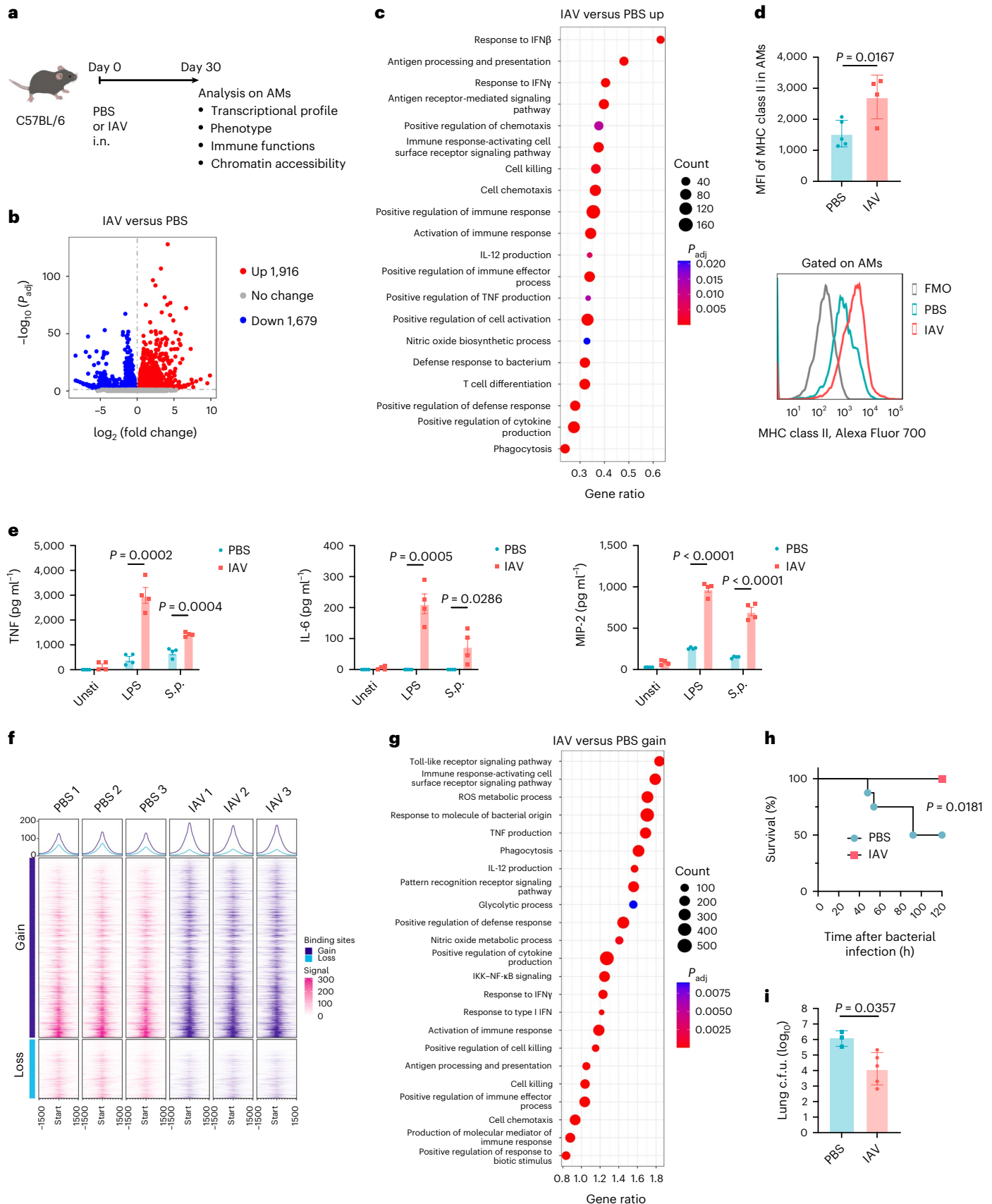
Fig. 2 | Virus-exposed AMs respond to tumors in the lungs. **a**, Schema of continuous CD4⁺ and CD8⁺ T cell depletion in IAV-infected mice inoculated i.v. with B16 melanoma cells. **b,c**, Macroscopic evaluation of the lungs (**b**) and number of macroscopically visible B16 tumor nodules on the surface of lung lobes after tumor inoculation from uninfected (PBS) or IAV-infected mice or IAV-infected mice with T cell depletion (IAV_{Tdepl}; **c**). **d,e**, Representative lung histopathology images (**d**) and percentage of lung area occupied by tumor lesions in mice shown in **b** (**e**). **f**, Schema of AM depletion in PBS-treated (PBS_{AMdepl}) and IAV-infected (IAV_{AMdepl}) mice at day 30 followed by inoculation of B16 melanoma cells in the lung. **g,h**, Macroscopic evaluation of the lungs (**g**) and number of macroscopically visible B16 tumor nodules on the surface of lung lobes after tumor inoculation from PBS- or IAV-infected mice with or without AM depletion (**h**). **i,j**, Representative lung histopathology images (**i**) and percentage of lung area occupied by tumor lesions in mice shown in **g** (**j**). **k**, Schema of

adoptive transfer of AMs isolated from PBS- or IAV-infected mice at day 30 i.t. into naive recipient mice followed by inoculation of B16 melanoma cells in the lungs of recipients. **l,m**, Luciferin-based in vivo tumor imaging (**l**) and average radiance of luciferin signals in the lung area in mice receiving PBS AMs or IAV AMs (**m**). **n,o**, Macroscopic evaluation of the lungs (**n**) and number of macroscopically visible B16 tumor nodules on the surface of lung lobes from mice shown in **l** (**o**). **p,q**, Representative lung histopathology images (**p**) and percentage of lung area occupied by tumor lesions in mice shown in **l** (**q**). Bar graphs are presented as mean ± s.d. Data are representative of two independent experiments, with the numbers of mice per group indicated ($n = 5$ mice per group in **c**, **e**, **h** and **j**; $n = 4$ PBS AM mice and $n = 5$ IAV AM mice in **m**, **o** and **q**). A two-tailed Student's *t*-test was performed for comparisons between two groups. A one-way ANOVA followed by a Tukey test was performed to compare more than two groups.

was consistently over 30% in both uninfected and IAV-infected mice (Fig. 4g,h). In sharp contrast, there was minimal chimerism (~1% on average) of AMs in either uninfected or day 30 IAV-infected mice

(Fig. 4i,j). By using an i.v. anti-CD45 staining strategy to exclude cells in the lung vasculature, we observed that chimerism of interstitial macrophages (IMs) in the lung interstitium was far higher than





that of AMs (Fig. 4k,l), supporting the monocytic ontogeny of IMs. These data indicate that IAV-trained AM generation is independent of monocytes.

IAV infection induced acute loss of AMs, with a nearly 90% reduction in AM cell number by around 1 week after infection, and the AM population started to recover between days 9 and 11 after infection

Fig. 3 | IAV infection induces trained immunity in AMs. **a**, Schema of respiratory IAV infection in mice and characterization of AMs on day 30 after infection. **b**, Volcano plots showing RNA transcripts differentially expressed (adjusted P value (P_{adj}) of <0.05 , $|\log_2(\text{fold change})| > 0$) in AMs from IAV-infected mice on day 30 after infection versus those from uninfected (PBS-treated) mice. **c**, GO enrichment of cluster-specific marker gene transcripts ($P_{\text{adj}} < 0.05$) related to immune functions that are upregulated in IAV versus PBS AMs. **d**, Mean fluorescence intensity (MFI) and representative flow cytometry histograms of MHC class II expression on PBS and day 30 IAV AMs. FMO, fluorescence minus one. **e**, Concentrations of representative proinflammatory cytokines/chemokines, including TNF, IL-6 and MIP-2, in supernatants of ex vivo cultured AMs either unstimulated (unsti) or stimulated with LPS or live *S. pneumoniae* (*S.p.*). **f**, ATAC-seq heat maps and metagene plots showing the top 1,000 genes with significant gain or loss (FDR < 0.017) of chromatin accessibility in IAV

versus PBS AMs. **g**, GO enrichment of ATAC-seq chromatin regions related to immune functions with significant ($P_{\text{adj}} < 0.05$) gain of chromatin accessibility in IAV versus PBS AMs. **h**, Survival of PBS- or IAV-infected mice after respiratory infection with *S. pneumoniae* at 5×10^7 c.f.u. per mouse on day 30 after viral infection. **i**, Bacterial burden (c.f.u.) in the lungs at 72 h after bacterial infection in PBS- or day 30 IAV-infected mice. Bar graphs are presented as mean \pm s.d. Data in **b**, **c**, **h** and **i** are representative of two independent experiments, data in **d** and **e** are representative of three independent experiments, and data in **f** and **g** are representative of one experiment, with numbers of mice per group as indicated ($n = 3$ per group in **b**, **c**, **f** and **g**; $n = 5$ PBS-treated mice and $n = 4$ IAV-infected mice in **d**; $n = 4$ culture wells per group in **e**; $n = 8$ per group in **h**; $n = 3$ PBS-treated mice and $n = 5$ IAV-infected mice in **i**). A two-tailed Student's t -test was performed for comparisons between two groups. A log-rank (Mantel–Cox) test was used for comparison of survival curves.

(Extended Data Fig. 1c). By using a similar parabiosis approach, we showed minimal chimerism in AMs even on day 9 after infection when niches of AMs were presumably vacant (Fig. 4m). These data point to the possibility that recovery of the AM population after IAV infection was achieved through autonomous proliferation of surviving embryonic-derived AMs. To analyze the proliferation status of AMs at this time point in situ, we performed BrdU incorporation analysis in AMs before infection and on days 9 and 11 after IAV infection. On average, around 10% of AMs incorporated BrdU before infection (Fig. 4n). On day 9 after infection, only 2% of AMs incorporated BrdU (Fig. 4n). Surprisingly, on day 11 after infection, as high as $>50\%$ of AMs incorporated BrdU (Fig. 4n). These data suggest that although IAV infection causes substantial loss of AMs, their numbers recover after resolution of acute inflammation via vigorous proliferation of IAV-exposed embryonic-derived resident AMs, through which tissue-specific trained immunity in AMs is generated.

Trained AMs have enhanced phagocytic and tumor cytotoxic functions

Previous studies suggest that tissue-resident macrophages represent a major source of TAMs and play key roles in oncogenesis in their respective tissues of residence, including the lung, liver and pancreas^{16,17,19}. We went on to address whether trained AMs infiltrate tumor lesions in the lung. By using confocal microscopy in immunostained lung sections, we observed abundant Siglec-F⁺CD11c⁺ AMs in juxtaposition with B16 melanoma cells in lung tumor lesions (Fig. 5a). Notably, there were higher numbers of tumor cell phagocytosis events by IAV-trained AMs than by IAV-naive (PBS) AMs (Fig. 5a). These data prompted us to hypothesize that trained AMs exert antitumor immunity via enhanced phagocytosis and/or tumoricidal functions. In support of this, RNA-seq in IAV AMs showed enhanced transcription of gene clusters related to phagocytosis, cell killing and the reactive oxygen species (ROS) biosynthetic process that are closely related to antitumor functions of macrophages (Fig. 5b–d). To further show the antitumor functions of trained AMs, we cocultured B16-luc cells with freshly isolated PBS or IAV AMs and assessed tumor cell survival (Fig. 5e–g). There were

significantly reduced numbers of live B16 cells cocultured for 72 h with IAV AMs compared to those cocultured with PBS AMs (Fig. 5e, f and Extended Data Fig. 6a). Analysis at different time points showed that antitumor effects of IAV AMs were only marginal at 24 h but were evident at 48 and 72 h of coculture (Fig. 5g).

We found that antitumor effects of IAV AMs were abrogated when AMs and tumor cells were separated by transwell (Fig. 5h), supporting contact-dependent tumor killing by trained AMs. However, treatment with anti-CD47 had minimal effects on antitumor functions of trained AMs (Fig. 5i), suggesting that enhanced tumor phagocytosis by trained AMs is independent of modulation of 'don't eat me' signals. By using flow cytometry analysis in a similar coculture of AMs and B16-GFP cells, we further showed that phagocytosis of tumor cells was significantly higher in IAV AMs than in PBS AMs (Fig. 5j). Confocal microscopy of AM–B16 coculture also showed increased phagocytic events by IAV AMs (Fig. 5k, l). Three-dimensional reconstruction of confocal microscopy images confirmed that B16 cells were truly engulfed by trained AMs (Fig. 5m). These data thus indicate that trained AMs exert antitumor functions via enhanced phagocytosis and killing of tumor cells.

To study whether trained AMs kill phagocytosed tumor cells via macrophage cell death, we measured potential cell death of PBS or IAV AMs cocultured with B16 cells for 48 h. There were no changes in Annexin V⁺propidium iodide⁺ (Annexin V⁺PI⁺) or Annexin V⁺PI⁻ AMs before versus after coculture, suggesting that tumoricidal functions in trained AMs are independent of AM cell death (Extended Data Fig. 6b). A recent study showed that enhanced fatty acid oxidation is essential for macrophage antitumor activity²⁴. We therefore asked whether enhanced mitochondrial oxidation in trained AMs (Extended Data Fig. 4g, h) is critical to their enhanced tumoricidal functions. We found that IAV AMs showed enhanced OCRs compared to PBS AMs both before and after coculture with B16 cells for 48 h (Extended Data Fig. 6c, d). To further show the significance of enhanced OCR in tumoricidal functions of trained AMs, we used etomoxir (an inhibitor of fatty acid oxidation) and UK5099 (an inhibitor of the glucose oxidation pathway) either alone or in combination to suppress mitochondrial oxidation in AMs (Extended Data Fig. 6e, f). Reduced tumor cell killing was

Fig. 4 | IAV-trained AMs develop independently of circulating monocytes.

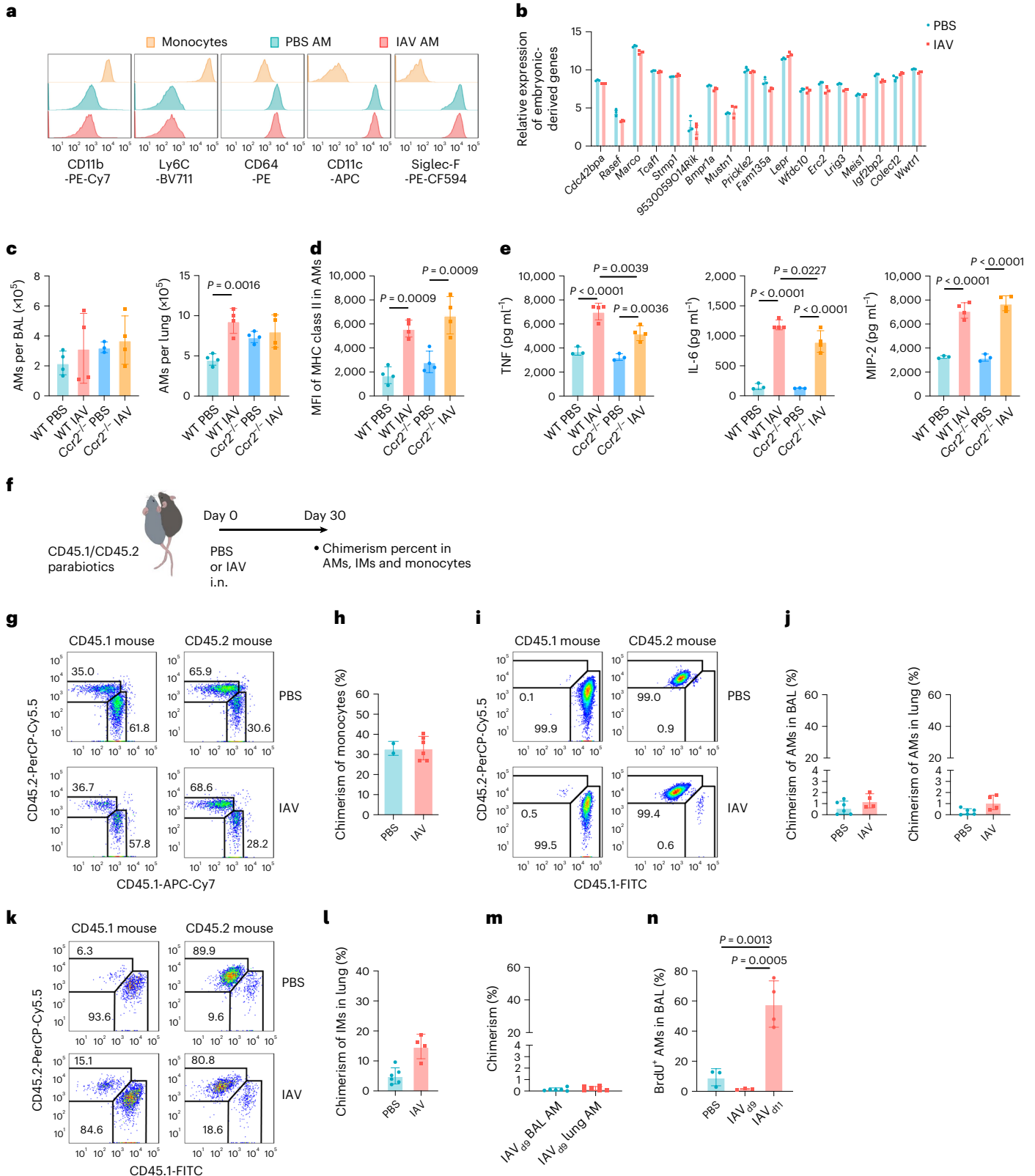
a, Representative flow cytometry histograms of surface molecules on peripheral blood monocytes and AMs from uninfected (PBS) or IAV-infected mice. **b**, Relative transcription levels of embryonic-derived signature genes in PBS or IAV AMs ($n = 3$ mice per group). **c**, Numbers of AMs in WT or *Ccr2*-knockout (*Ccr2*^{-/-}) mice on day 30 after IAV infection ($n = 3$ or 4 mice per group as indicated). **d**, MHC class II expression in PBS and day 30 IAV AMs in WT or *Ccr2*^{-/-} mice ($n = 4$ mice per group). **e**, Concentrations of representative cytokines/chemokines in supernatants of ex vivo cultured AMs stimulated with LPS ($n = 3$ or 4 culture wells per group as indicated). **f**, Schema of the parabiotic mouse model. **g, h**, Representative flow cytometry dot plots (**g**) and chimerism of circulating monocytes in PBS- or IAV-infected parabiotic mice (**h**; $n = 2$ PBS-treated mice and $n = 6$ IAV-infected mice). **i, j**, Representative flow cytometry dot plots of AMs in

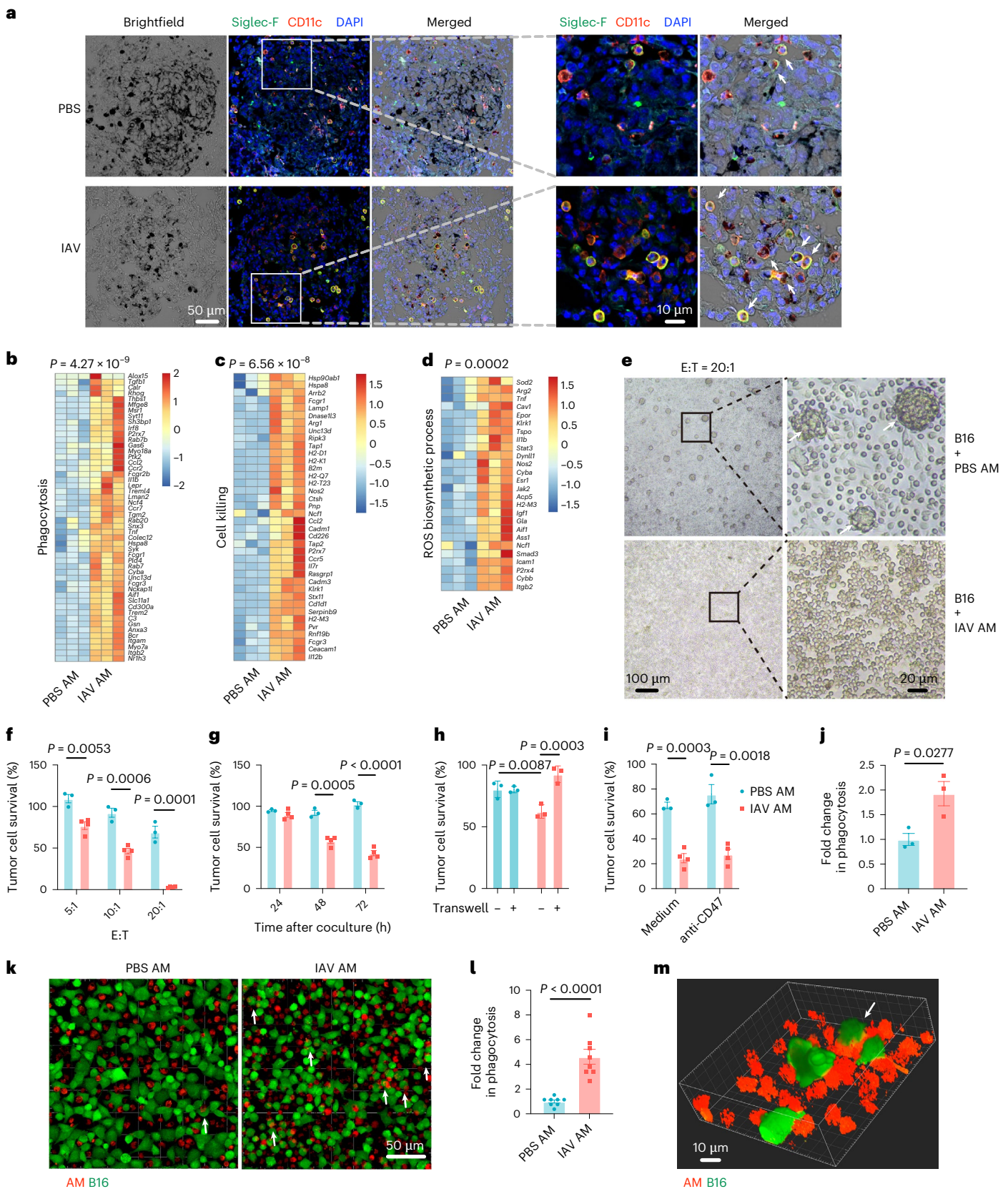
BAL samples (**i**) and chimerism of AMs in BAL samples and lungs of parabiotic mice (**j**). **k, l**, Representative flow cytometry dot plots (**k**) and chimerism of IMs in the lungs of parabiotic mice (**l**; $n = 6$ or 4 mice per group as indicated in **l**). **m**, Chimerism of AMs in BAL samples and lungs of PBS- or day 9 IAV-infected (IAV_{9s}) parabiotic mice ($n = 6$ mice per group). **n**, Percentage of BrdU-incorporating AMs in BAL samples of PBS- or IAV-infected mice on days 9 and 11 after infection ($n = 3$ or 4 mice per group as indicated); CD45⁺ cells by intravenous staining are shown in **l–m**. Numbers in **g**, **i** and **k** indicate percent against parental gate. Bar graphs are presented as mean \pm s.d. Data are representatives of two (**b–e** and **g–n**) or three (**a**) independent experiments. A two-tailed Student's t -test was performed for comparisons between two groups. A one-way ANOVA followed by a Tukey test was performed to compare more than two groups.

observed in the presence of etomoxir or UK5099 and was most evident with combined etomoxir and UK5099 treatment (Extended Data Fig. 6g). As reduced numbers of live B16 cells were observed after culture with etomoxir and/or UK5099 (Extended Data Fig. 6h), our data indicate that tumoricidal functions of IAV-trained AMs are dependent on enhanced mitochondrial oxidation from fatty acids and glucose.

Trained AMs are resistant to tumor-induced immunosuppression

Immunosuppression in TAMs induced by the tumor microenvironment represents a key mechanism in tumor immune escape. To functionally characterize trained AMs in such microenvironments during tumorigenesis in the lung tissues, AMs were purified after establishment of





B16 tumors in the lungs of PBS-treated or IAV-infected mice (Extended Data Fig. 7a,b) for ATAC-seq and RNA-seq analysis. ATAC-seq showed that in PBS-treated mice, lung tumors induced the loss of chromatin accessibility in 1,655 genes and the gain of accessibility in 888 genes (PBS-B16 versus PBS; Fig. 6a). Specifically, genes with gain of chromatin

accessibility included those related to negative regulation of immune functions, while genes with loss of chromatin accessibility included largely those associated with immune activation pathways (Fig. 6b,c). These changes in infection-free AMs indicate that tumor progress induced an immune-suppressive microenvironment in the lung.

Fig. 5 | Trained AMs have enhanced phagocytic and tumor cytotoxic functions. **a**, Representative confocal microscopic images on Siglec-F⁺CD11c⁺ AMs and melanoma cells (black colored cells in brightfield) in lung tumor lesions in PBS- or IAV-infected mice. Arrows indicate B16 cells phagocytosed by AMs. **b–d**, RNA-seq heat maps showing z scores of different gene transcripts ($P < 0.05$) related to phagocytosis, cell killing and ROS biosynthetic process in AMs from PBS- or IAV-infected mice. **e**, Representative microscopic images of B16 cells cocultured for 72 h with AMs isolated from PBS- or day 30 IAV-infected mice. Arrows indicate cellular clusters composed of B16 tumor cells and AMs. **f**, Survival of B16 cells cocultured at different AM:B16 (E:T) ratios with PBS or IAV AMs for 72 h. **g**, Survival of B16 cells at 24, 48 and 72 h after coculture with PBS or IAV AMs at an E:T ratio of 10:1. **h**, Survival of B16 cells cocultured with PBS or IAV AMs with or without separation of the two cell types by transwell insertions.

i, Survival of B16 cells cocultured with PBS or IAV AMs with or without pretreatment with monoclonal antibody to CD47. **j**, Relative phagocytosis of B16-GFP cells by PBS AMs versus IAV AMs as shown by flow cytometry analysis. **k, l**, Representative confocal microscopic images (**k**) and fold change (**l**) of phagocytosis of B16-GFP cells by AMs in coculture. **m**, Representative three-dimensional imaging of a B16-GFP cell phagocytosed by an IAV AM in coculture. Bar graphs are presented as mean \pm s.d. Data are representative of three independent experiments ($n = 5$ mice per group in **a**; $n = 3$ mice per group in **b–d**; $n = 3$ or 4 culture wells per group as indicated in **f, g** and **i**; $n = 3$ culture wells per group in **h** and **j**; $n = 8$ culture wells per group in **l**). A two-tailed Student's *t*-test was performed for comparisons between two groups. A one-way ANOVA followed by a Tukey test was performed to compare more than two groups, except in **h** where a two-way ANOVA was used.

Compared to PBS-B16 AMs, IAV-trained AMs in tumor-bearing lungs (IAV-B16) had a gain of chromatin accessibility in 6,516 genes and a loss of chromatin accessibility in 1,268 genes (Fig. 6d). KEGG enrichment of cluster-specific marker genes comparing IAV-B16 to PBS-B16 AMs showed a gain of chromatin accessibility of genes related to immune activation and trained immunity, in particular intracellular signaling pathways (Fig. 6e). Notably, GSEA for ATAC-seq signal changes of genes comparing IAV-B16 to PBS-B16 AMs showed enrichment of pathways closely related to antitumor trained immunity functions in AMs, including phagocytosis, cell killing, glycolysis process and reactive nitric oxide species metabolic process (Extended Data Fig. 7c–f), indicating enhanced antitumor functions in IAV versus PBS AMs in the tumor-bearing lung microenvironment. These data suggest that trained, but not naive, AMs are epigenetically resistant to the immune-suppressive microenvironment induced by lung tumors.

Heat map and correlation analyses based on RNA-seq data showed drastic changes in transcriptional profiles of PBS AMs after tumor establishment in the lung (PBS versus PBS-B16; Fig. 6f and Extended Data Fig. 7g). By contrast, fewer changes in transcriptional profiles were observed in trained AMs before than after tumor inoculation (IAV versus IAV-B16; Fig. 6f and Extended Data Fig. 7g). This is further supported by GO enrichment of gene clusters showing that immune activation-related gene transcripts (cluster C3) that were upregulated by IAV remain largely unchanged after tumor establishment in the lung (Fig. 6f,g). Specifically, IAV-upregulated gene transcripts associated with trained immunity and antitumor functions, including antigen processing and presentation, phagocytosis, the Toll-like receptor signaling pathway and nitric oxide biosynthesis process, remain essentially unchanged after tumor establishment (Fig. 6h). These data suggest that trained AMs are transcriptionally resistant to tumor-induced immune-suppressive microenvironments.

Antitumor trained immunity of AMs is dependent on interferon- γ (IFN γ) and natural killer (NK) cells

Our previous study showed that AdV-induced generation of trained immunity in AMs requires T cell help during the acute phase of the primary immune response via IFN γ -dependent mechanisms¹¹. We therefore asked whether IAV-induced antitumor trained immunity

in AMs also requires T cell help and/or IFN γ . To induce AMs that were not helped by T cells, we depleted both CD4⁺ and CD8⁺ T cells in vivo from day 3 after IAV infection to day 30 when B16 melanoma cells were inoculated i.v. (Fig. 7a). On day 17 after tumor inoculation, reduced tumor burden in the lungs was observed in IAV-infected mice regardless of T cell depletion (Fig. 7b–e), suggesting that T cell help is not required for IAV-induced antitumor trained immunity in AMs. To study the potential role of IFN γ , we infected *Irfng*-knockout mice (IFN γ ^{-/-}) and inoculated B16 melanoma cells i.v. on day 30 after infection (Fig. 7f). Tumor burden in the lungs was increased in IAV-infected IFN γ ^{-/-} mice compared to in uninfected mice (Fig. 7g–j). These data suggest that IFN γ is required for the enhanced antitumor functions of IAV-trained AMs.

Compared to WT mice, IFN γ ^{-/-} mice had reduced IAV viral burden in the lungs on day 3 and to a lesser extent on day 5 after infection (Extended Data Fig. 8a). To test whether impaired AM training in IFN γ ^{-/-} mice was due to a dose effect of IAV, we infected IFN γ ^{-/-} mice with IAV at either a standard dose (120 plaque-forming units (p.f.u.) per mouse) or a high dose (360 p.f.u. per mouse). High-dose IAV infection in IFN γ ^{-/-} mice failed to rescue the impaired antitumor functions in AMs (Extended Data Fig. 8b), arguing against an IAV dose effect in IFN γ ^{-/-} mice. Moreover, impaired AM training was consistently observed in *Irfng*-knockout (IFN γ ^{-/-}) mice (Fig. 7k and Extended Data Fig. 8c). These findings in AMs from both IFN γ ^{-/-} and IFN γ ^{-/-} mice strongly support a critical role of IFN γ signaling in IAV-induced antitumor trained AM generation.

To show the cellular source of IFN γ in IAV-infected lung tissues, we performed intracellular cytokine staining in lung leukocytes before and on days 3, 5 and 7 after infection. We identified NK cells as the dominant source of IFN γ on days 3 and 5 after infection, and T cells were not the major IFN γ producers until day 7 (Fig. 7l). With intact antitumor immunity in the lungs of T cell-depleted mice, we speculate that IFN γ -producing NK cells are critically required for IAV-induced antitumor trained AM generation. We therefore depleted NK cells or T cells in vivo in IAV-infected mice (Fig. 7m) and found that IAV-exposed AMs from NK-depleted, but not T cell-depleted, mice showed markedly reduced tumoricidal functions after coculture with B16-luc cells (Fig. 7n). Thus, these data collectively suggest that IFN γ and NK cells are required for IAV-induced antitumor trained immunity in AMs.

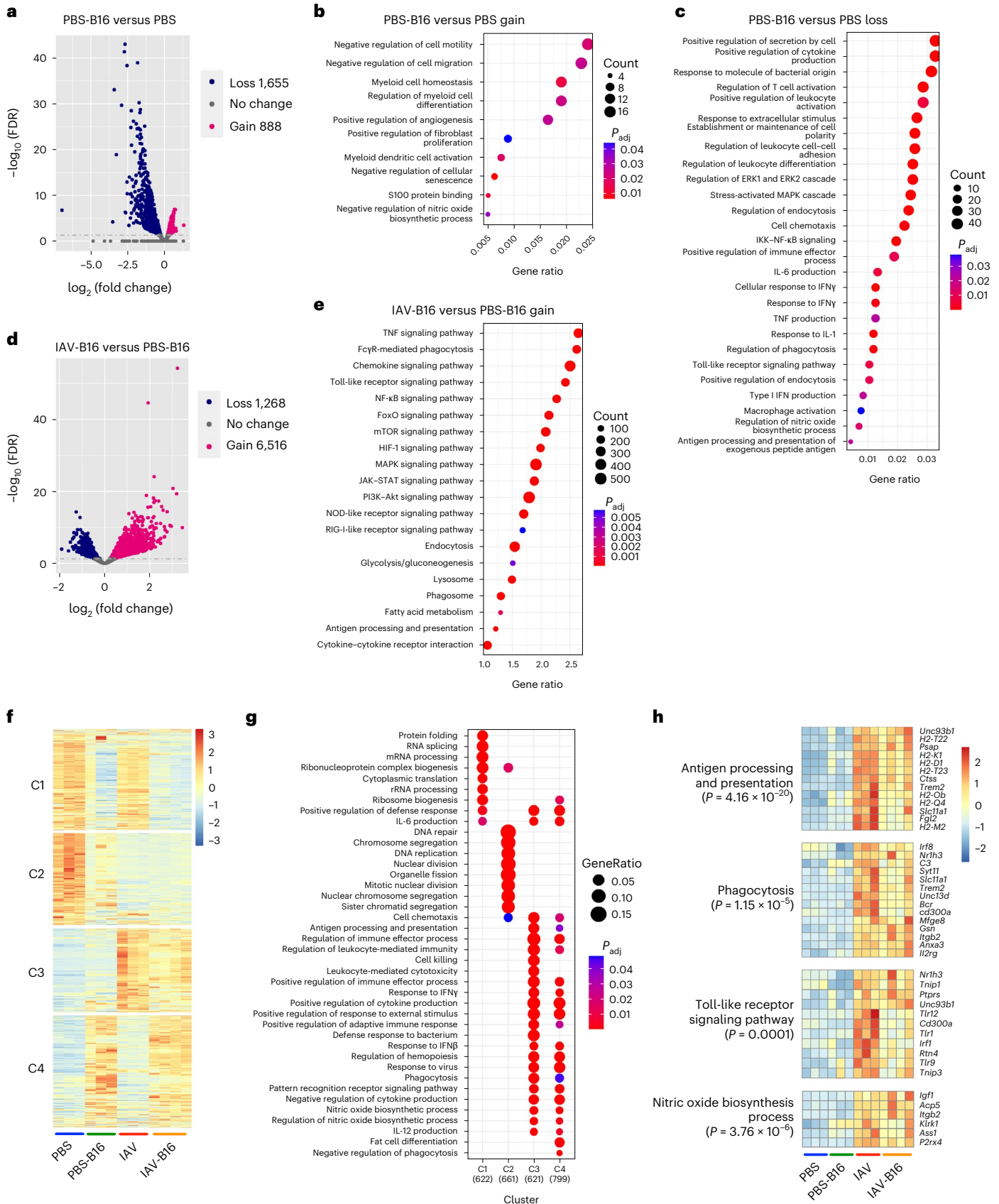
Fig. 6 | Trained AMs are resistant to tumor-induced immunosuppression.

a, ATAC-seq volcano plots showing genes with significant gain or loss (FDR < 0.05) of chromatin accessibility in AMs from uninfected tumor-bearing mice (PBS-B16) on day 9 after tumor inoculation versus naive (PBS) mice. **b**, GO enrichment of ATAC-seq chromatin regions related to immune suppression with significant ($P_{\text{adj}} < 0.05$) gain of chromatin accessibility in AMs from PBS-B16 versus PBS mice. **c**, GO enrichment of ATAC-seq chromatin regions related to immune activation with significant ($P_{\text{adj}} < 0.05$) loss of chromatin accessibility in AMs from PBS-B16 versus PBS mice. **d**, ATAC-seq volcano plots showing genes with significant gain or loss (FDR < 0.05) of chromatin accessibility in AMs from IAV-infected tumor-bearing mice (IAV-B16) versus PBS-B16 mice on day 9 after tumor inoculation. **e**, KEGG enrichment of ATAC-seq chromatin regions related

to immune activation with significant ($P_{\text{adj}} < 0.05$) gain of chromatin accessibility in AMs from IAV-B16 versus PBS-B16 mice. **f**, RNA-seq heat maps showing z scores of differentially expressed genes (gene transcripts with $P_{\text{adj}} < 0.05$ and $|\log_2(\text{fold change})| > 0$ are presented) in AMs from PBS, PBS-B16, IAV and IAV-B16 mice. AMs were isolated 9 d after tumor inoculation on day 30 after IAV infection. **g, h**, GO enrichment of cluster-specific marker genes in **f** (**g**) and RNA-seq heat maps showing z scores of differentially expressed genes ($P_{\text{adj}} < 0.05$) related to trained immunity and antitumor functions in AMs from the four experimental groups as shown in **f** (**h**). Data in **a–e** are from one experiment ($n = 3$ per group). Data in **f–h** are representative of two independent experiments ($n = 3$ or 4 per group as indicated). A hypergeometric test (one-sided with the Benjamini–Hochberg adjustment method) was used for statistical analysis in **b, c, e** and **g**.

Human trained AMs are associated with antitumor immunity
Our data thus far suggest that trained resident AMs play critical antitumor functions in the lungs in mice. We next sought to assess whether

trained resident AMs in human lung tumor tissues could also be identified and are associated with antitumor immunity. By using published original data on single-cell RNA-seq (scRNA-seq) in human non-small



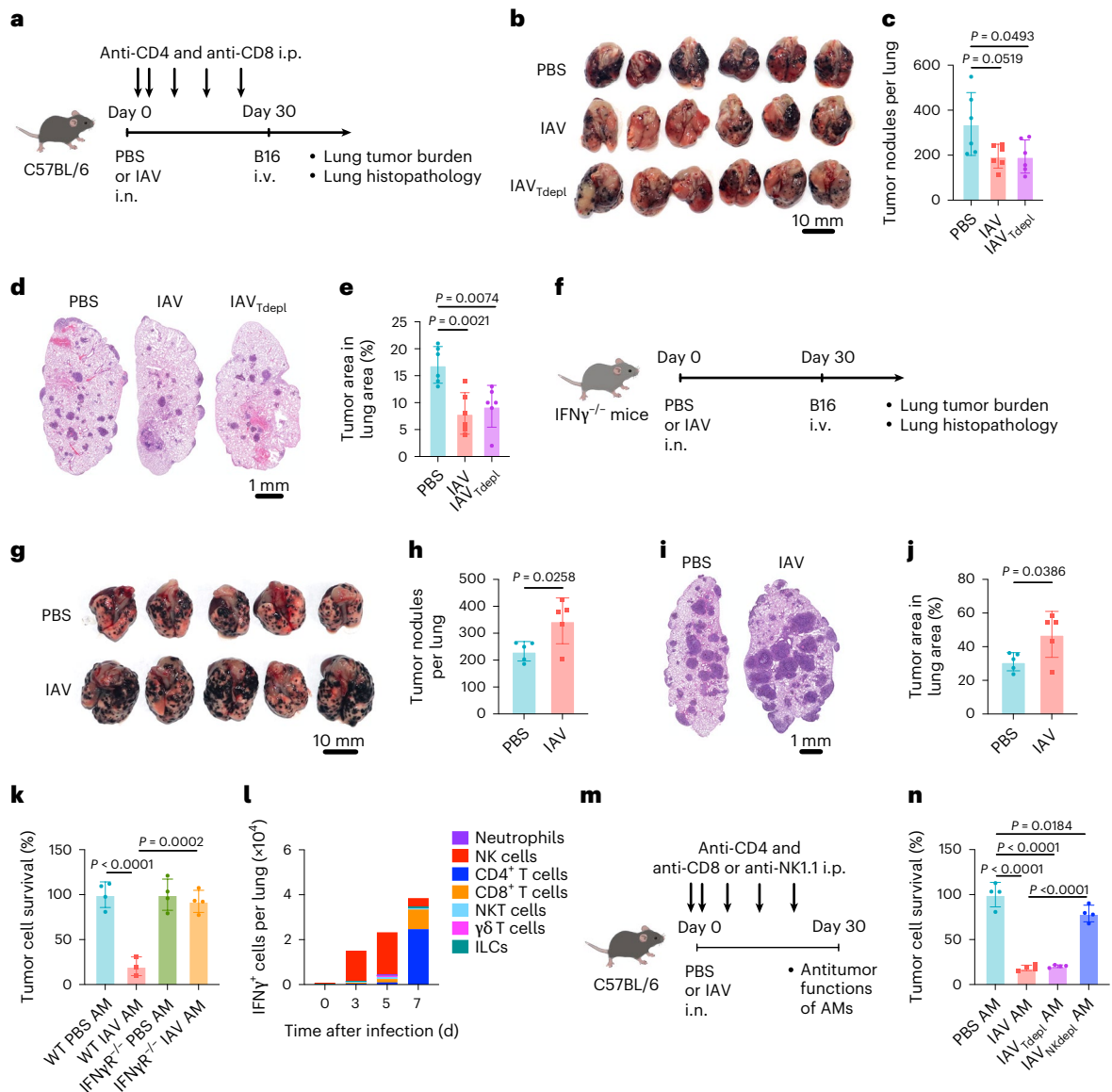


Fig. 7 | Antitumor trained immunity of AMs is dependent on IFN γ and NK cells. **a**, Schema of IAV infection in WT mice with continuous T cell depletion, followed by inoculation of B16 cells after infection. **b, c**, Macroscopic analysis of the lungs (**b**) and number of macroscopically visible B16 tumor nodules on the surface of lung lobes (**c**). **d, e**, Representative lung histopathology images (**d**) and percentage of lung area occupied by tumor lesions based on lung histopathological analysis in mice shown in **b** (**e**). **f**, Schema of IAV infection in *Ifng*-knockout (*IFN γ* ^{-/-}) mice followed by inoculation of B16 cells after infection. **g, h**, Macroscopic analysis of the lungs (**g**) and number of macroscopically visible B16 tumor nodules on the surface of lung lobes (**h**). **i, j**, Representative lung histopathology images (**i**) and percentage of lung area occupied by tumor lesions based on lung histopathological analysis in mice shown in **g** (**j**). **k**, Survival of

B16-luc cells cocultured for 72 h with AMs from PBS- or day 30 IAV-infected WT or *Ifng*-knockout (*IFN γ* ^{-/-}) mice. **l**, Number of IFN γ -producing leukocytes in the lung after IAV infection; ILCs, innate lymphoid cells. **m**, Schema of IAV infection in WT mice with continuous T cell or NK cell depletion to assess antitumor functions of AMs. **n**, Survival of B16-luc cells cocultured with AMs as shown in **m**. Bar graphs are presented as mean \pm s.d. Data are representative of two independent experiments ($n = 6$ mice per group in **c** and **e**; $n = 5$ mice per group in **h** and **j**; $n = 3$ or 4 culture wells per group as indicated in **k**; $n = 4$ culture wells per group in **n**). A one-way ANOVA followed by a Tukey test was performed to compare more than two groups. A two-tailed Student's *t*-test was performed for comparisons between two groups.

cell lung cancer (NSCLC) tissues³⁷, we identified multiple subsets of resident AMs based on coexpression of characteristic genes, including *PPARG* and *SERPINA1*, and genes encoding macrophage markers, including CD14, CD68 and MRC1 (clusters 1, 2, 4, 5, 10, 11, 12 and 20, Fig. 8a and Extended Data Fig. 9a)^{17,37}. Notably, cluster 1AMs demonstrated transcriptional profiles of prototypical trained immunity, which is highly comparable to IAV-trained mouse resident AMs (Figs. 8b–f and 3c). Specifically, trained AMs in human lung cancer tissues are enriched in gene clusters associated with response to microbes/microbial

components and cytokines, proinflammatory cytokine production, immune activation-associated signaling pathways, glycolysis, antigen processing and presentation, chemotaxis and so on (Fig. 8b,c,e). Importantly, the frequency of trained AMs was significantly higher in human lung cancer tissues with high immune activation than in those with low immune activation tumor microenvironments (immune activation^{hi} versus immune activation^{low}; Fig. 8g–i). Thus, these results suggest that trained resident AMs infiltrating human lung cancer tissues are associated with antitumor immunity.

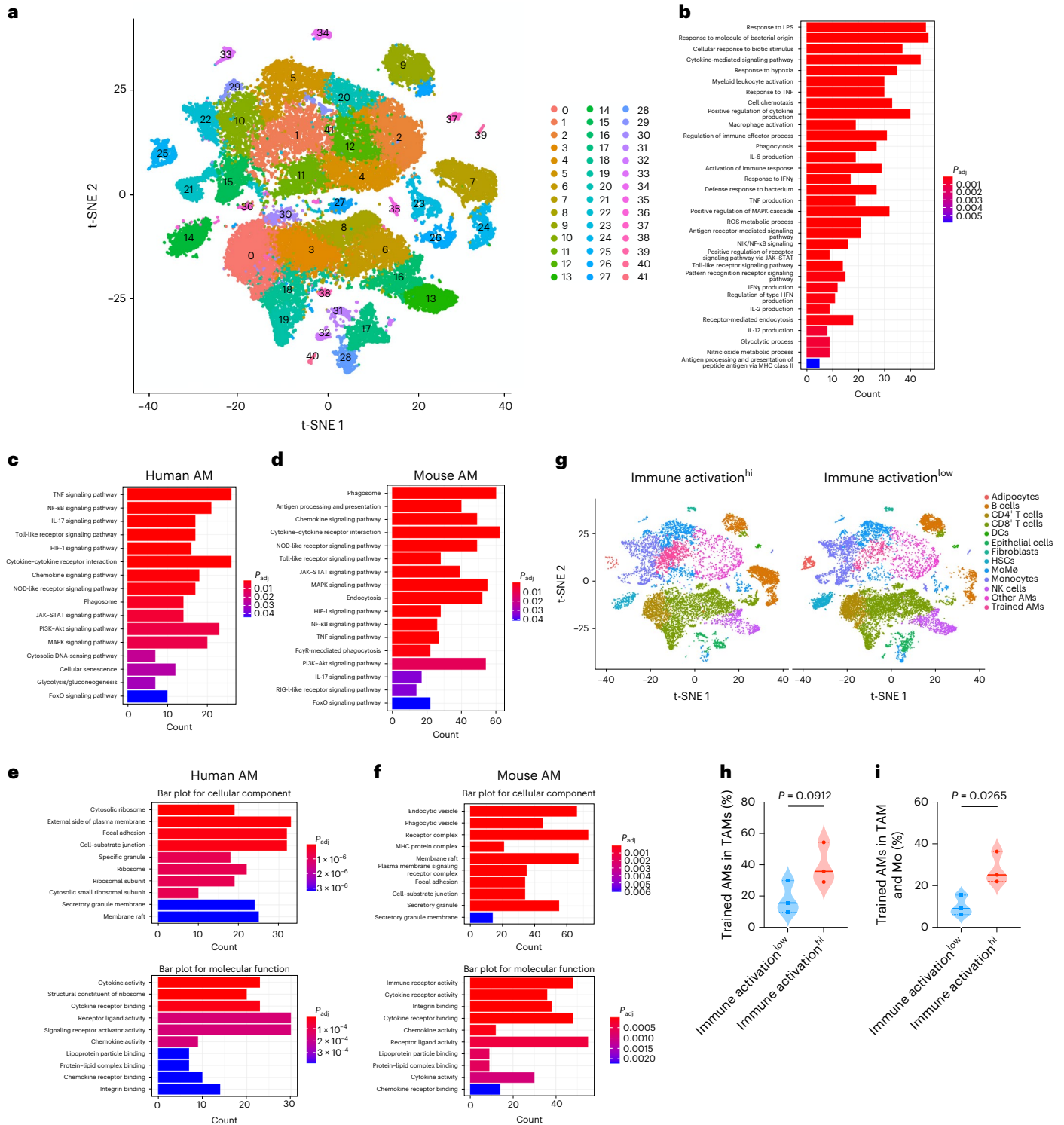


Fig. 8 | Human trained AMs are associated with antitumor immunity. **a**, scRNA-seq t-SNE plots showing a total of 42 cell populations in human NSCLC tumor tissues. **b**, GO enrichment of cluster-specific marker genes related to immune functions in human trained AMs. **c, d**, KEGG enrichment of cluster-specific marker genes related to immune activation signaling pathways in human (**c**) and mouse (**d**) trained AMs. **e, f**, GO enrichment of cluster-specific marker genes related to cellular components and molecular functions in human (**e**)

and mouse (**f**) trained AMs. **g**, scRNA-seq t-SNE plots showing the distribution of major cell populations in human NSCLC tumors with high or low immune activation; DCs, dendritic cells; HSCs, hematopoietic stem cells; MoMΦ, monocyte-derived macrophages. **h, i**, Percentage of trained AMs in total TAMs (**h**) and percentage of trained AMs in total TAMs and monocytes (Mo) in immune activation^{hi} and immune activation^{low} human NSCLC tumors (**i**). A two-tailed Student's *t*-test was performed for comparisons between two groups.

Discussion

Trained macrophages and monocytes are well recognized for their heterologous anti-infectious functions, as evidenced in both experimental animals and in humans^{10,13,32}. Nevertheless, functional significance of trained immunity during tumorigenesis remains far less appreciated. One relevant study using mouse subcutaneous tumor models reported trained neutrophils with systemic antitumor functions¹⁵. A more recent study showed that β -glucan, a widely used inducer of systemic trained immunity, attracts circulating monocyte influx into the pancreas to exert antitumor functions³⁸. Despite these intriguing findings, little is known about whether self-sustaining tissue-resident macrophages can carry antitumor trained immunity and exert long-term antitumor functions at specific tissue sites. Here, we show that lung tissue-resident trained AMs induced by acute respiratory viral infections are poised to exert long-lasting tissue-specific antitumor trained innate immunity. Mechanistically, trained AMs infiltrate tumor lesions and exert T cell-independent tumoricidal functions via enhanced engulfment and killing of tumor cells. Our study reveals a previously unappreciated role of tissue-specific antitumor trained innate immunity mediated by long-lasting and self-sustaining resident macrophages.

AMs originally derive from embryonic hematopoietic progenitor cells, and after birth, in particular during lung inflammation, these embryonic-derived AMs might be replaced by circulating monocytes to generate monocyte-derived AMs^{29,39}. We show in this study and in a previous study that acute respiratory infection by influenza virus or AdV, two common respiratory viral pathogens, induces trained immunity in self-sustaining embryonic-derived AMs long after resolution of the primary immune response¹¹. Our data are, however, contradictory with a previous study showing a monocytic ontogeny of antibacterial AMs following acute IAV infection³². A possible explanation is the myeloablative drug busulfan used in this previous study introduced additional cytotoxicity in resident AMs and therefore impaired their autonomous recovery after IAV infection^{32,40}. In support of our data, a previous study suggested that IAV infection does not deplete AMs in B6 mice⁴¹. Not unexpectedly, IAV infection in our study induced a drastic reduction in AM cell number by days 5 to 9 after infection, which started to recover by around day 11. We showed that on day 11 after infection, as high as >50% of surviving AMs incorporated BrdU, reflecting their robust proliferating status after resolution of acute IAV infection. Our data support the idea that AMs have potent self-sustaining potential, and thus training in embryonic-derived resident AMs may represent a generalized phenotype induced by acute respiratory viral infections.

The tumor-associated microenvironment drives TAMs toward protumor polarization early during tumor development via diversified mechanisms, including modulating signaling pathways and altering the production of effector mediators and epigenetic and/or metabolic programming⁴². With continuous influence of the microenvironment on TAMs, it is not unexpected that TAM-targeting therapeutic strategies to date rely largely on repeated administration of short-term effective TAM-modulating agents to antagonize the continuous taming by the tumor-associated microenvironment^{14,21,23,24}. Our data suggest that trained resident AMs are resistant to the tumor-associated immune-suppressive microenvironment at transcriptional and epigenetic levels at least until the middle stage of lung tumor development. By contrast, naive AMs are highly susceptible to such an immune-suppressive microenvironment, as demonstrated by loss of chromatin accessibility in genes related to immune activation. One of the limitations in our study is that we used peritumoral rather than intratumoral AMs for transcriptional and epigenetic analysis due to technical challenges in dissecting sporadic small tumor lesions across the lung. However, the drastic transcriptional and epigenetic changes in peritumoral AMs in tumor-bearing lungs indicate profound influences by tumors despite their peritumoral location^{43–45}. It is therefore plausible to speculate that the tumor-associated microenvironment educates not only tumor-infiltrating AMs but also peritumoral naive

AMs toward an immune-suppressive polarization, which may later infiltrate expanding tumor lesions. Thus, our data indicate that pre-established trained immunity in resident AMs endows an intrinsic resistance to tumor-associated immune-suppressive microenvironments, which is key for trained AMs to reserve antitumor polarization in immune-suppressive microenvironments. Although we show a markedly reduced lung tumor burden in IAV-exposed mice versus in IAV-naive mice, the survival time of the IAV-exposed mice was only 5 d longer than that of the IAV-naive mice. We speculate that this is due to the fast-growing nature of lung B16 tumors, in particular at later stages of tumor development. Moreover, antitumor immunity in IAV-exposed lungs is exerted by trained AMs via enhanced tumor cell phagocytosis without contribution from adaptive T cell-mediated antitumor immunity. These observations highlight the significance of comprehensive antitumor immunity mediated by both the innate and adaptive branches. Nevertheless, our study does not exclude the possibility that trained AMs may facilitate T cell-mediated antitumor immunity^{23,42,46}. Induction of trained immunity in tissue-resident macrophages thus represents an attractive strategy with durable antitumor effects.

We show here that trained AMs infiltrating lung tumor tissues are associated with antitumor immunity in humans. However, the causal factors that induce trained immunity in human NSCLC-infiltrating resident AMs remain speculative. A recent clinical study shows that aerosol delivery of AdV-vectored vaccine induces trained immunity in human AMs⁴⁷. Therefore, trained immunity in human AMs could, similar to that observed in mice, be induced by respiratory viral infections likely including influenza. Moreover, clinical evidence on the association between respiratory viral infections and lung cancers has been scarce. This may reflect sophisticated mechanisms in the modulation of the human respiratory immune environment overtime by a wide variety of stimulants far beyond viral infections, which deserve further investigation.

Our study shed light on tissue-resident macrophages as a potential target of trained immunity-based anticancer strategy, that is, prophylactic induction of trained antitumor immunity in resident AMs. Such a strategy is particularly appealing in individuals with extrapulmonary cancers, such as melanoma and breast cancer, which have high risks of lung metastasis. Our study will foster further investigation on the induction of trained immunity in tumor-infiltrating resident macrophages in a therapeutic setting, either as a monotherapy or in combination with T cell-based immunotherapies.

Online content

Any methods, additional references, Nature Portfolio reporting summaries, source data, extended data, supplementary information, acknowledgements, peer review information; details of author contributions and competing interests; and statements of data and code availability are available at <https://doi.org/10.1038/s41590-023-01428-x>.

References

1. Mitroulis, I. et al. Modulation of myelopoiesis progenitors is an integral component of trained immunity. *Cell* **172**, 147–161 (2018).
2. Cheng, S.-C. et al. mTOR- and HIF-1 α -mediated aerobic glycolysis as metabolic basis for trained immunity. *Science* **345**, 1250684 (2014).
3. Kaufmann, E. et al. BCG educates hematopoietic stem cells to generate protective innate immunity against tuberculosis. *Cell* **172**, 176–190 (2018).
4. Chen, F. et al. Neutrophils prime a long-lived effector macrophage phenotype that mediates accelerated helminth expulsion. *Nat. Immunol.* **15**, 938–946 (2014).
5. Dai, H. et al. PIRs mediate innate myeloid cell memory to nonself MHC molecules. *Science* **368**, 1122–1127 (2020).
6. Hole, C. R. et al. Induction of memory-like dendritic cell responses in vivo. *Nat. Commun.* **10**, 2955 (2019).

7. Jeyanathan, M. et al. Parenteral BCG vaccine induces lung-resident memory macrophages and trained immunity via the gut–lung axis. *Nat. Immunol.* **23**, 1687–1702 (2022).
8. Netea, M. G. et al. Trained immunity: a program of innate immune memory in health and disease. *Science* **352**, aaf1098 (2016).
9. Divangahi, M. et al. Trained immunity, tolerance, priming and differentiation: distinct immunological processes. *Nat. Immunol.* **22**, 2–6 (2021).
10. Netea, M. G. & Joosten, L. A. B. Trained immunity and local innate immune memory in the lung. *Cell* **175**, 1463–1465 (2018).
11. Yao, Y. et al. Induction of autonomous memory alveolar macrophages requires T cell help and is critical to trained immunity. *Cell* **175**, 1634–1650 (2018).
12. Lérias, J. R. et al. Trained immunity for personalized cancer immunotherapy: current knowledge and future opportunities. *Front. Microbiol.* **10**, 2924 (2019).
13. Giamarellos-Bourboulis, E. J. et al. Activate: randomized clinical trial of BCG vaccination against infection in the elderly. *Cell* **183**, 315–323 (2020).
14. Priem, B. et al. Trained immunity-promoting nanobiologic therapy suppresses tumor growth and potentiates checkpoint inhibition. *Cell* **183**, 786–801 (2020).
15. Kalafati, L. et al. Innate immune training of granulopoiesis promotes anti-tumor activity. *Cell* **183**, 771–785 (2020).
16. Zhu, Y. et al. Tissue-resident macrophages in pancreatic ductal adenocarcinoma originate from embryonic hematopoiesis and promote tumor progression. *Immunity* **47**, 323–338 (2017).
17. Casanova-Acebes, M. et al. Tissue-resident macrophages provide a pro-tumorigenic niche to early NSCLC cells. *Nature* **595**, 578–584 (2021).
18. Sharma, S. K. et al. Pulmonary alveolar macrophages contribute to the premetastatic niche by suppressing antitumor T cell responses in the lungs. *J. Immunol.* **194**, 5529–5538 (2015).
19. Sheng, J. et al. Topological analysis of hepatocellular carcinoma tumour microenvironment based on imaging mass cytometry reveals cellular neighbourhood regulated reversely by macrophages with different ontogeny. *Gut* **71**, 1176–1191 (2021).
20. Altorki, N. K. et al. The lung microenvironment: an important regulator of tumour growth and metastasis. *Nat. Rev. Cancer* **19**, 9–31 (2019).
21. Feng, M. et al. Phagocytosis checkpoints as new targets for cancer immunotherapy. *Nat. Rev. Cancer* **19**, 568–586 (2019).
22. Jaynes, J. M. et al. Mannose receptor (CD206) activation in tumor-associated macrophages enhances adaptive and innate antitumor immune responses. *Sci. Transl. Med.* **12**, eaax6337 (2020).
23. Ingram, J. R. et al. Localized CD47 blockade enhances immunotherapy for murine melanoma. *Proc. Natl Acad. Sci. USA* **114**, 10184–10189 (2017).
24. Liu, M. et al. Metabolic rewiring of macrophages by CpG potentiates clearance of cancer cells and overcomes tumor-expressed CD47-mediated ‘don’t-eat-me’ signal. *Nat. Immunol.* **20**, 265–275 (2019).
25. Zhou, Y. et al. Blockade of the phagocytic receptor MerTK on tumor-associated macrophages enhances P2X7R-dependent STING activation by tumor-derived cGAMP. *Immunity* **52**, 357–373 (2020).
26. Hirsch, F. R. et al. Lung cancer: current therapies and new targeted treatments. *Lancet* **389**, 299–311 (2017).
27. Headley, M. B. et al. Visualization of immediate immune responses to pioneer metastatic cells in the lung. *Nature* **531**, 513–517 (2016).
28. Nguyen, D. X., Bos, P. D. & Massagué, J. Metastasis: from dissemination to organ-specific colonization. *Nat. Rev. Cancer* **9**, 274–284 (2009).
29. Kopf, M., Schneider, C. & Nobs, S. P. The development and function of lung-resident macrophages and dendritic cells. *Nat. Immunol.* **16**, 36–44 (2015).
30. Jeyanathan, M. et al. Immunological considerations for COVID-19 vaccine strategies. *Nat. Rev. Immunol.* **20**, 615–632 (2020).
31. Alon, R. et al. Leukocyte trafficking to the lungs and beyond: lessons from influenza for COVID-19. *Nat. Rev. Immunol.* **21**, 49–64 (2021).
32. Aegerter, H. et al. Influenza-induced monocyte-derived alveolar macrophages confer prolonged antibacterial protection. *Nat. Immunol.* **21**, 145–157 (2020).
33. Damjanovic, D. et al. Negative regulation of lung inflammation and immunopathology by TNF- α during acute influenza infection. *Am. J. Pathol.* **179**, 2963–2976 (2011).
34. Shibuya, T. et al. Immunoregulatory monocyte subset promotes metastasis associated with therapeutic intervention for primary tumor. *Front. Immunol.* **12**, 663115 (2021).
35. Huh, S. J., Liang, S., Sharma, A., Dong, C. & Robertson, G. P. Transiently entrapped circulating tumor cells interact with neutrophils to facilitate lung metastasis development. *Cancer Res.* **70**, 6071–6082 (2010).
36. Machiels, B. et al. A gammaherpesvirus provides protection against allergic asthma by inducing the replacement of resident alveolar macrophages with regulatory monocytes. *Nat. Immunol.* **18**, 1310–1320 (2017).
37. Leader, A. M. et al. Single-cell analysis of human non-small cell lung cancer lesions refines tumor classification and patient stratification. *Cancer Cell* **39**, 1594–1609 (2021).
38. Geller, A. E. et al. The induction of peripheral trained immunity in the pancreas incites anti-tumor activity to control pancreatic cancer progression. *Nat. Commun.* **13**, 759 (2022).
39. Hashimoto, D. et al. Tissue-resident macrophages self-maintain locally throughout adult life with minimal contribution from circulating monocytes. *Immunity* **38**, 792–804 (2013).
40. Hubbard, L. L. N., Ballinger, M. N., Wilke, C. A. & Moore, B. B. Comparison of conditioning regimens for alveolar macrophage reconstitution and innate immune function post bone marrow transplant. *Exp. Lung Res.* **34**, 263–275 (2008).
41. Califano, D., Furuya, Y. & Metzger, D. W. Effects of influenza on alveolar macrophage viability are dependent on mouse genetic strain. *J. Immunol.* **201**, 134–144 (2018).
42. DeNardo, D. G. & Ruffell, B. Macrophages as regulators of tumour immunity and immunotherapy. *Nat. Rev. Immunol.* **19**, 369–382 (2019).
43. Zheng, X. et al. Spatial density and distribution of tumor-associated macrophages predict survival in non-small cell lung carcinoma. *Cancer Res.* **80**, 4414–4425 (2020).
44. Movahedi, K. et al. Different tumor microenvironments contain functionally distinct subsets of macrophages derived from Ly6C^{high} monocytes. *Cancer Res.* **70**, 5728–5739 (2010).
45. Doak, G. R., Schwertfeger, K. L. & Wood, D. K. Distant relations: macrophage functions in the metastatic niche. *Trends Cancer* **4**, 445–459 (2018).
46. Netea, M. G., Joosten, L. A. B. & van der Meer, J. W. M. Hypothesis: stimulation of trained immunity as adjunctive immunotherapy in cancer. *J. Leukoc. Biol.* **102**, 1323–1332 (2017).
47. Jeyanathan, M. et al. Aerosol delivery, but not intramuscular injection, of adenovirus-vectored tuberculosis vaccine induces respiratory-mucosal immunity in humans. *JCI Insight* **7**, e155655 (2022).

Publisher's note Springer Nature remains neutral with regard to jurisdictional claims in published maps and institutional affiliations.

Springer Nature or its licensor (e.g. a society or other partner) holds exclusive rights to this article under a publishing agreement with

the author(s) or other rightsholder(s); author self-archiving of the accepted manuscript version of this article is solely governed by the terms of such publishing agreement and applicable law.

© The Author(s), under exclusive licence to Springer Nature America, Inc. 2023

Methods

Mice

WT female C57BL/6 mice and BALB/c mice were purchased from Slac Laboratory Animals. CD45.1⁺ mice (B6.SJL-*Ptprc^a Pepc^b*/BoyJ), *Ifng*-knockout mice (B6.129S7-*Ifng^{tm1Ts}*/J) and *Ccr2*-knockout mice (B6.129S4-*Ccr2^{tm1Jc}*/J) were originally from the Jackson Laboratory and were kind gifts from Z. Cai (Zhejiang University), X. Wang (Soochow University) and H. Tang (Shandong First Medical University), respectively. *Ifngr*-knockout mice on a C57BL/6 background were generated by GemPharmatech and were a kind gift from S. Zhu (Zhejiang University). Mice were housed in a specific pathogen-free facility with ad libitum access to food (Xietong Shengwu) and water and were maintained on a 12-h light/12-h dark cycle, with 50–60% humidity and at 20–25 °C at Zhejiang University Laboratory Animal Center. Animals were assigned experimental groups at random. Female mice at 6–8 weeks of age were used for all experiments, and the numbers of mice per experimental group are indicated in the figure legends. All experiments were performed in accordance with the guidelines from the Animal Research and Ethics Boards of Zhejiang University.

Respiratory viral and extracellular bacterial infections

Acute respiratory viral infection was introduced by i.n. administration of influenza virus (A/PR8/34; 120 p.f.u. per mouse) or recombinant human serotype 5 AdV (2×10^7 p.f.u. per mouse)¹¹. In selected experiments, mice were infected with IAV at 360 p.f.u. per mouse. Mice were anesthetized with isoflurane and infected i.n. with 25 μ l of virus preparation in PBS. Respiratory infection with extracellular bacteria was introduced by i.t. administration of *S. pneumoniae* serotype 3 (ATCC, 6303) resuspended in 40 μ l of PBS at 2×10^7 or 5×10^7 colony-forming units (c.f.u.) per mouse as indicated. Growth of *S. pneumoniae* was assessed as previously described¹¹. Briefly, frozen bacterial stock was plated on blood tryptic soy agar supplemented with 5% defibrinated sheep blood (YC Biotech) and 10 mg ml⁻¹ neomycin (Sigma-Aldrich) and incubated overnight. Bacterial colonies were cultured at 37 °C and 5% CO₂ in Todd Hewitt broth (BD Biosciences).

Mouse tumor models

The GFP-expressing B16F10 cell line (B16-GFP) was generated from luciferase-expressing B16F10 cells (B16-luc; ATCC, CRL-6475-LUC2) by transduction with lentiviral vector encoding GFP under the EF-1 α promoter. B16F10 (B16; ATCC, CRL-6475), B16-luc and B16-GFP cells were grown in RPMI 1640 cell culture medium (Thermo Fisher) supplemented with 10% fetal bovine serum (Serana) and 1% penicillin/streptomycin (Biosharp). A total of 5×10^5 B16 cells were resuspended in 200 μ l of PBS and injected i.v. to establish lung melanoma or injected s.c. to the right flank. To establish a spontaneous lung metastasis model, 5×10^5 4T1 (ATCC, CRL-2539) cells resuspended in 100 μ l of PBS were injected into the fourth mammary fat pad on the right side of BALB/c mice. The s.c. tumor volume was calculated as volume = (length \times width²)/2. A maximal tumor size of 15 mm for the longest axis of the tumor was accepted and was always observed during this study.

Luciferin-based in vivo tumor imaging

Mice were anesthetized with isoflurane and injected intraperitoneally (i.p.) with 150 mg kg⁻¹ D-luciferin (Yeason Biotechnology). After injection, mice were placed on the imaging platform of an IVIS Spectrum imaging station (PerkinElmer) with continuous isoflurane inhalation. White light and luciferase activity were recorded for 40 s starting at 8 min after D-luciferin injection. Living Image software (PerkinElmer) was used for luciferase activity quantification.

Lung macroscopic analysis and histopathology

Lung lobes were collected between days 15 and 18 after tumor inoculation. Visible B16 tumor nodules on the surface of all lung lobes were counted under a JSZ8 dissection microscope (Jiangnan Novel Optics).

In selected experiments, lung vascular perfusion was performed to remove erythrocytes for further immunohistochemical analysis of lung sections. Lung lobes were then either processed for frozen fixation or were paraffin embedded. Paraffin-embedded lung sections with hematoxylin and eosin or Masson's Trichrome staining were scanned on a VS200 research slide scanner (Olympus) by using VS200 ASW software (Olympus) for further analysis.

Confocal microscopy

Frozen or paraffin-embedded lung tissue sections were incubated with 5% bovine serum albumin plus 5% normal goat serum in PBS for 1 h at 37 °C for blocking, followed by incubation with primary antibodies at 4 °C overnight and on the following day with secondary antibodies for 1 h at room temperature. Mounting was performed by using DAPI Fluoromount-G (SouthernBiotech) according to manufacturer's instructions. For staining of Siglec-F, anti-mouse Siglec-F (clone IRNM44N, Thermo Fisher) was used as primary antibody, followed by staining with goat anti-rat AF488 (Thermo Fisher). Anti-mouse CD11c AF647 (clone N418, Biolegend) was used for CD11c staining. Confocal microscopy was performed on a Zeiss LSM 880 confocal microscope (Zeiss), and quantification of fluorescence intensity was performed using ImageJ software and ZEN Black imaging software (Zeiss). Z-stack reconstruction was performed using Imaris software version 9.0.1 (Oxford Instruments).

Isolation of cells from peripheral blood and lung tissues

Cells from peripheral blood, bronchoalveolar lavage (BAL) and lung tissues were isolated as previously described¹¹. Briefly, mice were anesthetized with isoflurane, and peripheral blood was exhaustively collected from the abdominal vein. Following exhaustive BAL with PBS, lung lobes were collected, cut into small pieces and digested in collagenase type I (Thermo Fisher) for 1 h at 37 °C in a shaker incubator. Lung single-cell suspensions were obtained by crushing the digested lung tissues through a 100- μ m basket filter (BD Biosciences). Following erythrocyte lysis of peripheral blood and lung cells by incubation with red blood cell lysing buffer (SolarBio), cells were washed with PBS and resuspended in desired medium for further experiments.

Flow cytometry

Immunostaining and flow cytometry analyses were performed as previously described¹¹. Briefly, single-cell suspensions from BAL, the lungs and peripheral blood were plated in U-bottom 96-well plates at $\leq 2 \times 10^6$ cells per well in PBS. Cells were stained with a Zombie Aqua fixable viability kit (Biolegend) according to manufacturer's instructions. Cells were then washed and incubated with anti-CD16/CD32 (clone 2.4G2, BD Biosciences, 1:200) in PBS containing 0.5% bovine serum albumin for 15 min on ice and stained with fluorochrome-labeled antibodies, including anti-CD45 APC-Cy7 (clone 30-F11, BD Biosciences, 1:400), anti-CD45.1 APC-Cy7 (clone A20, BD Biosciences, 1:200), anti-CD45.1 FITC (clone A20, Biolegend, 1:200), anti-CD45.2 PerCP-Cy5.5 (clone 104, Biolegend, 1:200), anti-CD11b PE-Cy7 (clone M1/70, BD Biosciences, 1:400), anti-CD11b BV605 (clone M1/70, Biolegend, 1:500), anti-CD11c APC (clone N418, Biolegend, 1:200), anti-CD11c PE-Cy7 (clone N418, Biolegend, 1:200), anti-I-A/I-E Alexa Fluor 700 (clone M5/114.15.2, Biolegend, 1:200), anti-CD3 V450 (clone 17A2, BD Biosciences, 1:200), anti-CD3 PE-CF594 (clone 17A2, Biolegend, 1:400), anti-CD49b PE (clone DX5, BD Bioscience, 1:400), anti-TCR α /TCR β PE-Cy7 (clone H57-597, Biolegend, 1:200), anti-TCR γ /TCR δ FITC (clone GL3, Biolegend, 1:200), anti-CD45R V450 (clone RA3-6B2, BD Bioscience, 1:200), anti-F4/80 PE-Cy7 (clone BM8, Biolegend, 1:200), anti-Ly6C BV711 (clone HK1.4, Biolegend, 1:500), anti-Ly6G-BV650 (clone 1A8, Biolegend, 1:500), anti-CD24-BV605 (clone M1/69, Biolegend, 1:500), anti-CD64-PE (clone X54-5/7.1, BD Biosciences, 1:200), anti-Siglec-F PE-CF594 (clone E50-2440, BD Biosciences, 1:500), anti-CD4 PE-Cy7 (clone RM4-5, BD Biosciences, 1:200), anti-CD8-APC-Cy7 (clone

53-6.7, BD Bioscience, 1:400), anti-FcεR1a PE-Cy7(clone MAR-1, eBioscience, 1:200), anti-Gata3 PE (clone TWAJ, eBioscience, 1:200), Lin (anti-mouse CD3ε, clone I45-2C11; anti-mouse Ly6G/Ly6C, clone RB6-8C5; anti-mouse CD11b, clone MI/70; anti-mouse CD45R/B220, clone RA3-6B2; anti-mouse TER-119/erythroid cells, clone Ter-119, Biolegend; 1:200) and streptavidin Percp-Cy5.5 (eBioscience, 1:200). In selected experiments, cells were stained with Annexin V and PI (both from MultiSciences) according to the manufacturer's instructions to measure cell death.

For i.v. staining, 2 μg of anti-CD45 APC-Cy7 (clone 30-F11, BD Biosciences) diluted in 100 μl of PBS was injected i.v. via the tail vein of anesthetized mice. Organs were collected 3 min after injection.

For intracellular staining of IFNγ, lung cells were cultured ex vivo in the presence of BD GolgiPlug (BD Biosciences) for 5 h, followed by cell surface staining as mentioned above. Cells were then fixed and permeabilized with fixation/permeabilization buffer (Thermo Fisher) and washed twice with 1× permeabilization buffer (Thermo Fisher), followed by intracellular staining with anti-IFNγ APC (clone XMGL2, Biolegend, 1:200) diluted in permeabilization buffer for 0.5 h at room temperature.

To analyze in situ AM proliferation, i.p. administration of BrdU was performed repeatedly at designated time points after influenza virus infection at 0.5 mg per mouse per injection. Before infection or on days 9 and 11 after infection, BAL and lung cells from mice receiving BrdU were labeled with the above extracellular antibodies, followed by intracellular staining of BrdU by using an APC BrdU flow kit (BD Biosciences) according to manufacturer's instructions. Briefly, cells stained with extracellular antibodies were fixed and permeabilized with BD Cytofix/Cytoperm and incubated with BD Cytoperm Plus buffer. Cells were refixed with BD Cytofix/Cytoperm before treatment with DNase. Incorporated BrdU was then stained with a monoclonal antibody to BrdU-APC (clone B44, BD Biosciences, 1:50).

Stained cells were analyzed on a BD LSRFortessa flow cytometer by using FACS Diva software (version 8.0.1, BD Biosciences). Data were analyzed and illustrated by using FlowJo software (version 10.7.1, BD Biosciences).

Parabiotic mouse model

Parabiotic surgery was conducted as previously described¹¹. Briefly, the mirroring lateral sides of two age- and weight-matched anesthetized mice (CD45.1⁺ and CD45.2⁺, respectively) were shaved, and skin incisions from elbow to knee joints on the respective mirroring sides were made. The adjacent elbow and knee joints and the dorsal and ventral skin were respectively approximated by sutures. Carprofen and buprenorphine were administered i.p. on days 0 to 3 of surgery. Three weeks after surgery, both mice were treated with PBS or IAV i.n. as described above. On days 9 and 30 after viral infection, chimerisms in peripheral blood monocytes and lung macrophages were measured by flow cytometry analysis. Chimerism was respectively calculated as percent CD45.1⁺/(percent CD45.1⁺ + percent CD45.2⁺) in CD45.2⁺ mice and as percent CD45.2⁺/(percent CD45.2⁺ + percent CD45.1⁺) in CD45.1⁺ mice.

BM transplantation

To generate BM chimeric mice, BM cells were collected from uninfected or day 30 IAV-infected CD45.1⁺ donor mice. A total of 2 × 10⁶ BM cells were transplanted i.v. into lethally irradiated (8.5 Gy) naive syngeneic host mice (CD45.2⁺). Five weeks after transplantation, recipient mice were inoculated with B16-luc melanoma cells i.v. as described above.

Purification, adoptive transfer and ex vivo stimulation of AMs

Purification, adoptive transfer and ex vivo stimulation of AMs were performed as previously described¹¹. To obtain purified AMs, BAL cells from naive or IAV-infected mice were labeled with CD11c microbeads (Miltenyi) followed by positive magnetic selection on a magnetic

purification system (Miltenyi) according to the manufacturer's instructions. Purified AMs were used for RNA-seq, ATAC-seq, adoptive transfer or ex vivo cell culture experiments. For adoptive transfer experiments, pooled AMs from multiple mice from the same treatment group were resuspended at 1 × 10⁶ AMs per recipient in 40 μl of PBS and were administered i.t. into isoflurane-anesthetized mice. For ex vivo stimulation of AMs, isolated AMs were stimulated with live *S. pneumoniae* (ATCC) at a multiplicity of infection of 10, as previously described¹¹, or with LPS at 10 ng ml⁻¹ and incubated for 12 h before supernatants were collected.

Coculture of AMs and tumor cells for antitumor activity assay

AMs were isolated as described above and were seeded in a 96-well tissue culture plate at 0.5 × 10⁵ to 2 × 10⁵ cells per well. Cells were incubated in a cell culture incubator (37 °C and 5% CO₂) for 2 h. B16-luc or B16-GFP tumor cells were seeded in AM culture wells at 1 × 10⁴ cells per well. At 24, 48 or 72 h of coculture, cells in each well were lysed, and luciferase activity per well was measured by using a luciferase assay system (Yeason Biotechnology), according to manufacturer's instructions. Luminescence measurements were performed on a SynergyMx M5 plate reader (Molecular Devices). Tumor cell survival was calculated and presented as percentage of normalized luminescence against tumor-only culture wells. In selected experiments, tumor cells were incubated with 10 μg ml⁻¹ rat anti-mouse CD47 (clone Miap301, Biolegend) at 37 °C for 20 min before coculture with AMs. In transwell experiments, AMs and B16-luc cells were cocultured in 24-well tissue culture plates, and in selected wells, AMs were separated from tumor cells by using transwell inserts with a pore size of 0.4 μm (Corning). In selected experiments, AMs and B16-luc cells were cocultured in the presence of 20 μM etomoxir and/or 20 μM UK5099 (both from MedChemExpress).

AM phagocytosis assay

Isolated AMs were seeded in a 96-well tissue culture plate at 5 × 10⁴ cells per well. B16-GFP cells were seeded in AM culture wells at 8 × 10⁴ cells per well. At 24 h after coculture, cells were washed and detached using 0.25% trypsin for 10 min. Single-cell suspensions were collected and stained with anti-CD11c-APC (clone N418, Biolegend) to label AMs, followed by flow cytometry analysis.

For fluorescence imaging assays, AMs were seeded in 35-mm glass-like polymer coverslip dishes at 4 × 10⁵ cells per dish. After 2 h of culture in a cell culture incubator (37 °C and 5% CO₂), AMs were labeled with 5 μM 1,1'-dioctadecyl-3,3',3'-tetramethylindocarbocyanine perchlorate (Beyotime) according to manufacturer's instructions. B16-GFP cells were then seeded in the culture dishes at 8 × 10⁴ cells per dish. After a further 24 h of coculture, confocal microscopy was performed on a Zeiss LSM 880 confocal microscope (Zeiss). Multiple random fields were collected per replicate, and the number of phagocytic events was scored for each replicate.

In vivo cell depletions

To deplete CD4⁺ T and CD8⁺ T cells in vivo, mice were injected i.p. with 200 μg of anti-CD4 (clone GK1.5, BioXCell) and 200 μg of anti-CD8 (clone 2.43, BioXCell). To deplete NK cells, mice were injected i.p. with 200 μg of anti-NK1.1 (clone PK136, made in-house). To achieve continuous T cell or NK cell depletion, repeated doses of 100 μg of depleting antibodies were administered at 7-d intervals through the endpoint of the experiment. To deplete AMs in vivo, a single dose of clodronate liposomes or control liposomes (Liposoma Technology) was administered i.t. to mice at 100 μl per mouse in two split doses. To deplete circulating monocytes in vivo, mice receiving i.t. clodronate/control liposomes were injected i.v. with clodronate or control liposomes, respectively, at 100 μl per mouse per d at 5-d intervals starting from 2 d after the initial i.t. dose of liposomes to the endpoint of the experiment.

Enzyme-linked immunosorbent assay (ELISA)

ELISAs were performed by using mouse TNF, IFN γ , IL-6 and MIP-2 ABTS ELISA development kits (Peprotech) or a mouse IFN β ELISA kit (InvivoGene), according to manufacturers' instructions. ELISA plates were read on a SynergyMx M5 plate reader (Molecular Devices). Concentrations of cytokines/chemokines were calculated based on serial dilutions of standards by using GraphPad Prism software (version 9, GraphPad software).

AM metabolic assays

Real-time cell metabolism of AMs was measured by using the Seahorse XF Cell Mito stress test kit or a Seahorse XF glycolytic stress test kit (Agilent Technologies) according to the manufacturer's instructions. After culture alone or coculture with B16 melanoma cells for 48 h, AMs were collected and purified by positive selection using CD11c microbeads (Miltenyi Biotec). Purified AMs were then seeded into XF 96-well plates (Agilent Technologies) at 50,000 cells per well and cultured overnight in complete RPMI 1640 medium. The next day, AMs were washed and incubated for 1 h in Seahorse assay medium (Agilent Technologies) supplemented with either 2 mM glutamine (glycolytic stress test) or an additional 10 mM glucose and 1 mM pyruvate (mito stress test). The kit compounds were resuspended in assay medium, and the final concentrations of the compounds in culture wells were 1.5 μ M oligomycin, 4 μ M FCCP and 0.5 μ M rotenone/antimycin A in the mito stress test or 10 mM glucose, 1 μ M oligomycin and 50 mM 2-DG in the glycolytic stress test. OCRs and ECARs were measured on a Seahorse XFe96 analyzer (Agilent Technologies), and data were analyzed using Wave Desktop software (v2.6).

Real-time quantitative PCR with reverse transcription (RT-PCR)

Total RNA was extracted from tissues using TRIzol reagent (Thermo Fisher). RT-PCR was performed by using a PrimeScript RT master mix for RT-PCR, according to the manufacturer's instructions (TaKaRa). IAV in infected lungs was quantified by real-time PCR of the influenza *NS1* gene in cDNA prepared from whole lung tissues. Quantification of B16 melanoma cells in organs was performed by real-time PCR of genes encoding premelanosome (*Pmel*), dopachrome tautomerase (*Dct*)³⁴ and luciferase. The expression of genes was normalized to that of *Actb*. The following primer sequences were used (Tsingke Biotechnology): *Pmel* (forward: 5'-GCTTGTAGGTATCTTGCTGGTGT-3', reverse: 5'-CCTGCTTCTAAGTCTATGCCTATG-3'), *Dct* (forward: 5'-GGCTACAATTACGCCGTTG-3', reverse: 5'-CACTGAGAGAGTTGTGGACCAA-3'), luciferase (forward: 5'-CACCGTCGTATTCTGTAGCA-3', reverse: 5'-AGTCGTACTCGTTGAAGCCG-3'), *NS1* (forward: 5'-GTCAAGCTTTCAGGTAGATTG-3', reverse: 5'-CTCTTAGGGATTCTGATCTC-3') and *Actb* (forward: 5'-AGTGTGACGTTGACATCCGT-3', reverse: 5'-GCAGCTCAGTAACAGTCCGC-3').

RNA-seq and data analysis

A total of 400,000 purified AMs per replicate were pelleted and lysed in TRIzol reagent (Thermo Fisher) and cryopreserved at -80 °C, followed by RNA extraction. RNA quantification and qualification were performed using an N50 NanoPhotometer microvolume spectrophotometer (IMPLEN) and an RNA Nano 6000 assay kit of the Bioanalyzer 2100 system (Agilent Technologies). Sequencing libraries were prepared using an NEBNext Ultra RNA library prep kit (New England Biolabs) following manufacturer's recommendations, and index codes were added to attribute sequences to each sample. Clustering of the index-coded samples was performed on a cBot cluster generation system using a TruSeq PE cluster kit v3-cBot-HS (Illumina), according to the manufacturer's instructions. After cluster generation, library preparations were sequenced on an Illumina Novaseq platform (Illumina).

Raw RNA-seq fastq format data were processed through in-house Perl scripts, and clean data were obtained by removing reads

containing adapter or poly(N) and low-quality reads from raw data. Reads were then mapped to mm10 RefSeq genes downloaded from the University of California Santa Cruz Table Browser using HISAT2 (v2.0.5). FeatureCounts (v1.5.0-p3) was used to count the read numbers mapped to each gene. Fragments per kilobase per million base pairs sequenced values of each gene were calculated based on the length and read counts mapped to the gene. A principal-component analysis (PCA) plot was generated, and differential gene expression analysis was performed by using the DESeq2 (v1.34.0) package in R (v4.1.2). The resulting *P* values were adjusted using the Benjamini-Hochberg approach for controlling the false discovery rate (FDR). An adjusted *P* value of <0.05 found by DESeq2 was used as the significance threshold for identification of differentially expressed genes. Volcano and heat map plots were created using the ggplot2 (v3.3.6) and pheatmap (v1.0.12) packages separately in R. GO enrichment analyses of differentially expressed genes were performed using the clusterProfiler R package (v4.2.1). GO terms with corrected *P* values of <0.05 were considered significantly enriched. ClusterProfiler (v4.2.1) was used to test the statistical enrichment of differentially expressed genes in KEGG pathways. The local version of the GSEA analysis tool (<http://www.broadinstitute.org/gsea/index.jsp>), GO and the KEGG dataset were used for GSEA independently.

ATAC-seq and data analysis

A total of 50,000 purified AMs per replicate were washed once in cold PBS and resuspended in 50 μ l of cold lysis buffer (10 mM Tris-HCl (pH 7.4), 10 mM NaCl, 3 mM MgCl₂ and 0.1% IGEPAL CA-630). Cell lysates were centrifuged at 500g for 10 min at 4 °C, and nuclei were resuspended in 50 μ l of transposition reaction mix (25 μ l of TD buffer, 2.5 μ l of Tn5 transposase and 22.5 μ l of nuclease-free water; Illumina) and incubated for 30 min at 37 °C. Transposed DNA fragments were purified by using a Qiagen Reaction MiniElute kit (Qiagen) barcoded with Nextera single indexes (New England Biolabs) and amplified by PCR for 11 cycles using NEBNext high fidelity 2 \times PCR master mix (New England Biolabs). PCR products were purified using a PCR purification kit (Qiagen), and amplified fragment size was verified on an Agilent 2100 Bioanalyzer system (Agilent). ATAC-seq libraries were quantified by quantitative PCR. Paired-end sequencing was performed on an Illumina Novaseq6000 system (Novogene).

Raw ATAC-seq fastq files from paired-end sequencing were trimmed by using Fastp (v0.19.11) followed by quality control using fastqc (v0.11.5). Clean data were aligned to the GRCm38/mm10 reference genome using BWA (v0.7.12-r1039). Samtools (v1.11) was used to remove unmapped, unpaired and mitochondrial reads. PCR duplicates were removed by using Picard (v1.111). Peak calling was performed using MACS2 (v2.1.2, -q 0.05 -call-summits -nomodel -shift -100 -extsize 200 -keep-dup all). For each experiment, peaks of all samples were combined to create a union peak list, and overlapping peaks were merged with BedTools (v2) merge. The number of reads in each peak was analyzed using DiffBind (v3.4). Differentially accessible peaks were identified following DESeq2 normalization using an FDR cutoff of <0.05. Tracks were visualized using Integrative Genomics Viewer (v2.3.77, Broad Institute). Pearson correlations and PCAs between samples were calculated in R (DiffBind v3.4) and plotted. GO term enrichment was performed for each biological condition using clusterProfiler (v4.2.1). Statistical analysis of differential chromatin accessibility tests was done using DESeq2 (v1.34.0), and FDR correction was performed using the Benjamini-Hochberg method in R (v4.1.2). Significance of GO term enrichments was calculated with binomial tests and hypergeometric tests. *P* values and *q* values of <0.05 were considered to indicate a significant difference.

Analysis of public human NSCLC scRNA-seq dataset

scRNA-seq data of tumors from six individuals with NSCLC (ID numbers 371, 408, 570, 571, 328 and 393) were downloaded from the Gene

Expression Omnibus (GEO) with accession code [GSE154826](#). The Seurat package (v4.1.0) was used for count normalization. Samples were filtered for cell barcodes recording >500 unique molecular identifiers, with <25% mitochondrial gene expression. Batch integration was initiated using the Seurat function `FindIntegrationAnchors()`. Neighbor analysis was performed by invoking `FindNeighbors()` using the default k parameter of 20 and the first 40 principal components. Clustering was then performed with `FindClusters()` at a resolution of 2 (resulting in 42 clusters). A PCA was performed based on the scaled data with the top 2,000 highly variable genes, and the top 40 principal components were used for t-distributed stochastic neighbor embedding (t-SNE) construction. Cell-type marker genes were found using the `FindConservedMarkers()` function.

Annotation of human NSCLC scRNA-seq clusters

Cell clusters were first annotated with `SingleR` (v1.8.1) `BlueprintEncodeData()` and confirmed by identifying differentially expressed marker genes for each cluster and comparing to known cell-type-specific marker genes from `CellMarker` (<http://bio-bigdata.hrbmu.edu.cn/CellMarker/>). Macrophages (clusters 1, 2, 4, 5, 10, 11, 12, 20, 23, 29, 36 and 41) expressed genes encoding CD14, CD68 and MRC1 and lacked PPARG. AMs (clusters 1, 2, 4, 5, 10, 11, 12 and 20) expressed genes encoding PPARG, SERPINA1 and MRC1.

Differential expression testing of human NSCLC scRNA-seq dataset

Differential expression between two sets of cells was performed using the `FindMarkers` function in the Seurat package (v4.1.0). GO and KEGG analyses of genes upregulated and downregulated in expression were performed using `clusterProfiler` (v4.2.1).

Statistical analysis

Statistical parameters, including the exact value of n , the definition of center, dispersion and precision measures and statistical significance, are reported in the figures and figure legends. A P value of <0.05 was considered significant. A two-tailed Student's t -test was performed for comparisons between two groups. A one-way analysis of variance (ANOVA) followed by a Tukey test was performed to compare more than two groups. A log-rank (Mantel–Cox) test was used for comparison of survival curves. All statistical analyses were performed using GraphPad Prism software (version 9, GraphPad software). The same samples were not repeatedly measured, and no data points were excluded from the analysis. The confidence interval was set at 95% for statistical analysis. No statistical methods were used to predetermine sample sizes, but our sample sizes are similar to those reported in previous publications^{7,11}. Data distribution was assumed to be normal, but this was not formally tested. Data collection and analysis were not performed blind to the conditions of the experiments.

Reporting summary

Further information on research design is available in the Nature Portfolio Reporting Summary linked to this article.

Data availability

RNA-seq data and ATAC-seq data have been deposited in the NCBI's GEO under accession code [GSE222150](#). Human scRNA-seq data were previously published³⁷ and can be accessed under accession code [GSE154826](#). Source data are provided with this paper.

Code availability

Code was generated using publicly available R (v4.1.2) packages, including `DESeq2`, `ggplot2`, `dplyr`, `pheatmap`, `clusterProfiler`, `Seurat`, `SingleR`, `tidyverse`, `patchwork`, `DiffBind`, `ChIPseeker`, `corrplot`, `ggridges` and `enrichplot`. No custom software was used or developed in this study. Analysis scripts will be provided upon request.

Acknowledgements

This work was supported by National Natural Science Foundation of China (31970861 and 32170893 to Y. Yao and 32100714 to Y.W.) and Natural Science Foundation of Zhejiang Province (LR20H100001 to Y. Yao). We thank Z. Xing (McMaster University) and Q. Wang (Zhejiang University) for proofreading the manuscript and helpful discussion. We thank X. Cao and Z. Guo (National Key Laboratory of Medical Immunology), J. Wang, Q. Wang, F. Xu, X. Wang, Z. Cai, S. Zhu and W. Lin (Zhejiang University), H. Tang (Shandong First Medical University), X. Wang (Soochow University) and J. Wang (Shanghai Jiao Tong University) for providing experimental materials or technical assistance. We thank C. Zhang, F. Wang and Y. Pan (all from Zhejiang University) for technical assistance. We thank Y. Li and Y. Xing from the Core Facilities of Zhejiang University School of Medicine for technical assistance.

Author contributions

T.W. and Y. Yao conceived and designed the study. T.W., J.Z., Y.W., Y.L., L.W., Y. Yu and Y. Yao performed experiments. T.W. and Y. Yao analyzed the data and wrote the paper.

Competing interests

The authors declare no competing interests.

Additional information

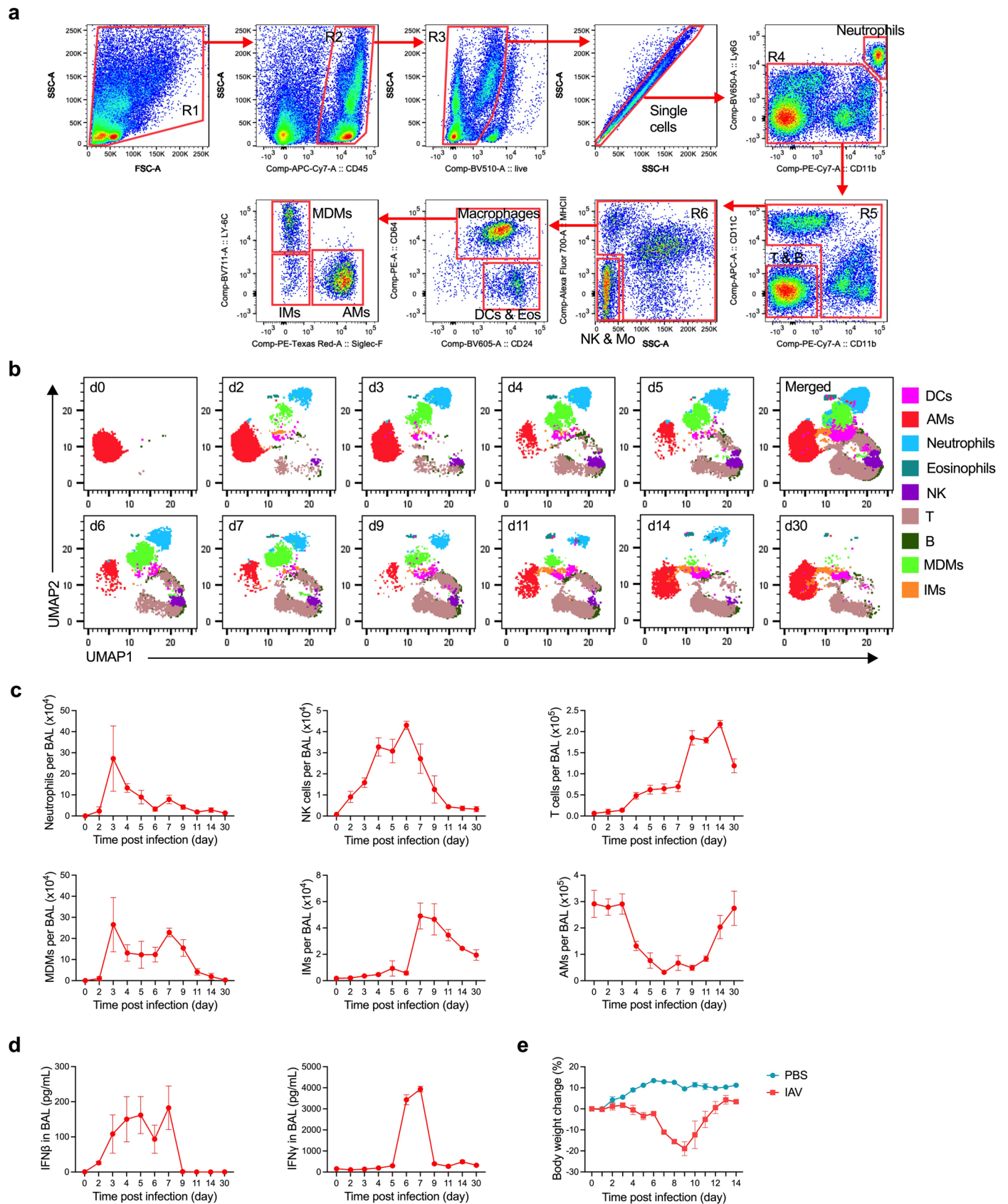
Extended data is available for this paper at <https://doi.org/10.1038/s41590-023-01428-x>.

Supplementary information The online version contains supplementary material available at <https://doi.org/10.1038/s41590-023-01428-x>.

Correspondence and requests for materials should be addressed to Yushi Yao.

Peer review information *Nature Immunology* thanks Maziar Divangahi and the other, anonymous, reviewer(s) for their contribution to the peer review of this work. Primary Handling Editor: N. Bernard, in collaboration with the *Nature Immunology* team. Peer reviewer reports are available.

Reprints and permissions information is available at www.nature.com/reprints.

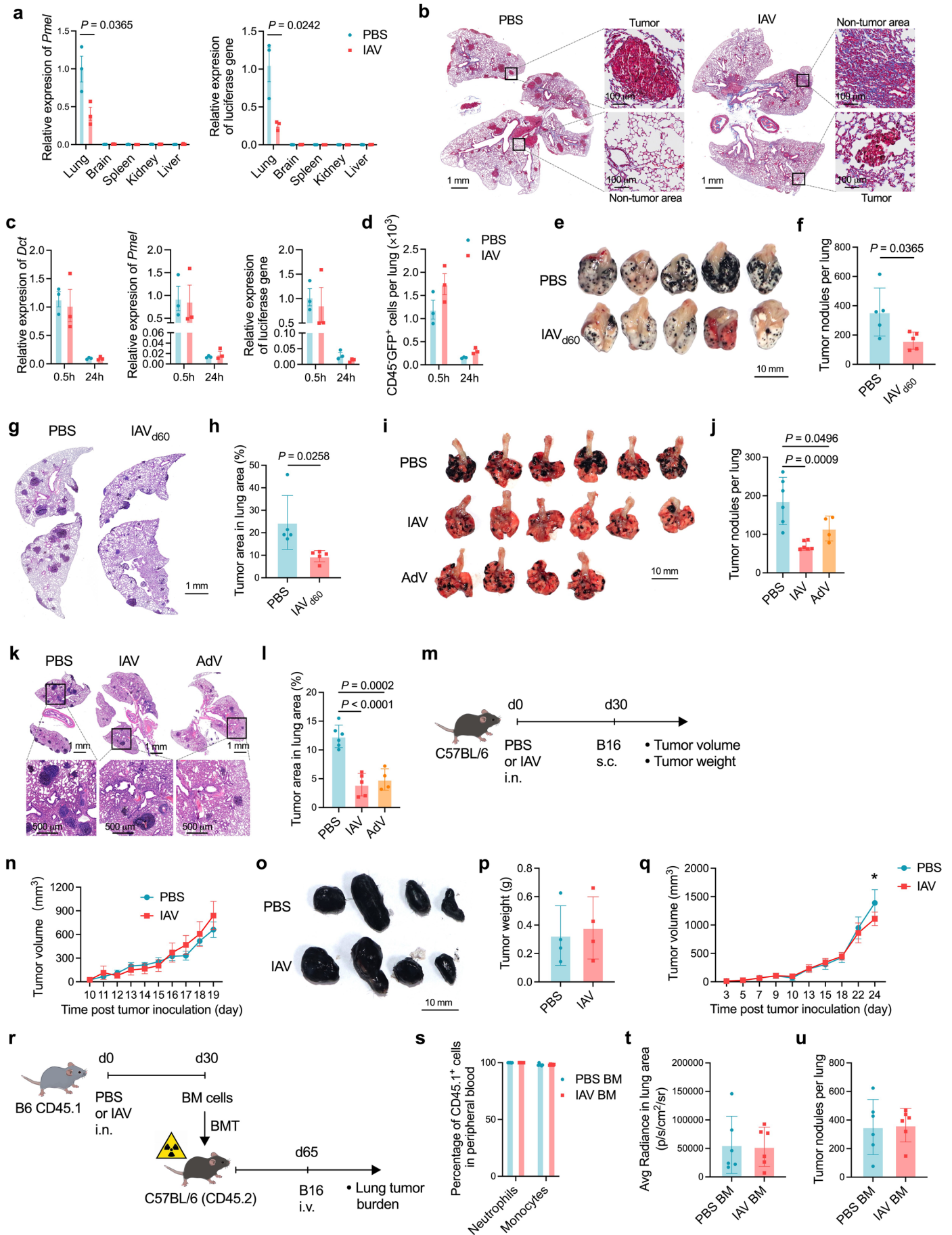


Extended Data Fig. 1 | See next page for caption.

Extended Data Fig. 1 | IAV infection induces acute respiratory inflammation.

(a) Representative flow cytometry dot plots showing gating strategy of leukocyte subsets including neutrophils, T and B lymphocytes, NK cells, monocytes (Mo), dendritic cells (DCs), eosinophils (Eos), alveolar macrophages (AMs), interstitial macrophages (IMs), and monocyte-derived macrophages (MDMs), in lung tissues of IAV-infected mice. (b) Representative UMAP plots on kinetic changes in leukocyte subsets in bronchoalveolar lavage fluid (BAL) from before to 30 days

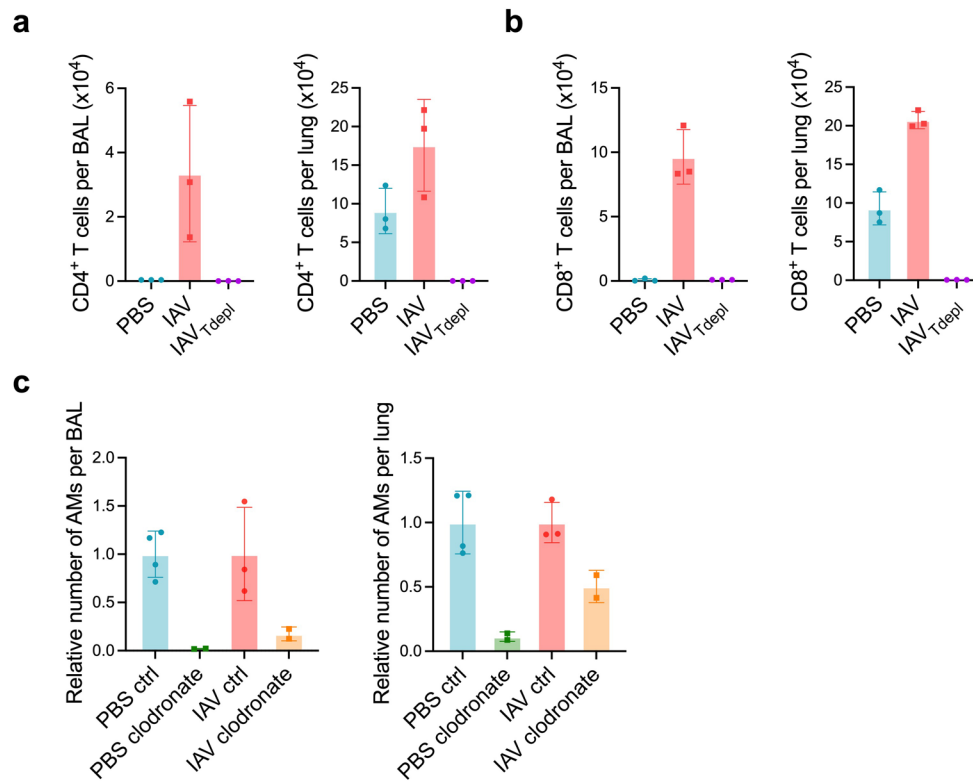
(d0 to d30) post IAV infection. (c) Kinetic changes in absolute numbers of selected leukocyte subsets in BAL post IAV infection. (d) Kinetic changes in IFN β and IFN γ in BAL supernatant post IAV infection. (e) Kinetic body weight change in IAV-infected mice. Data are presented as mean \pm SD. Data are representative of three independent experiments with n = 3 mice per group in a–c, n = 3 or 4 mice per group in d, and n = 2 mice per group in e.



Extended Data Fig. 2 | See next page for caption.

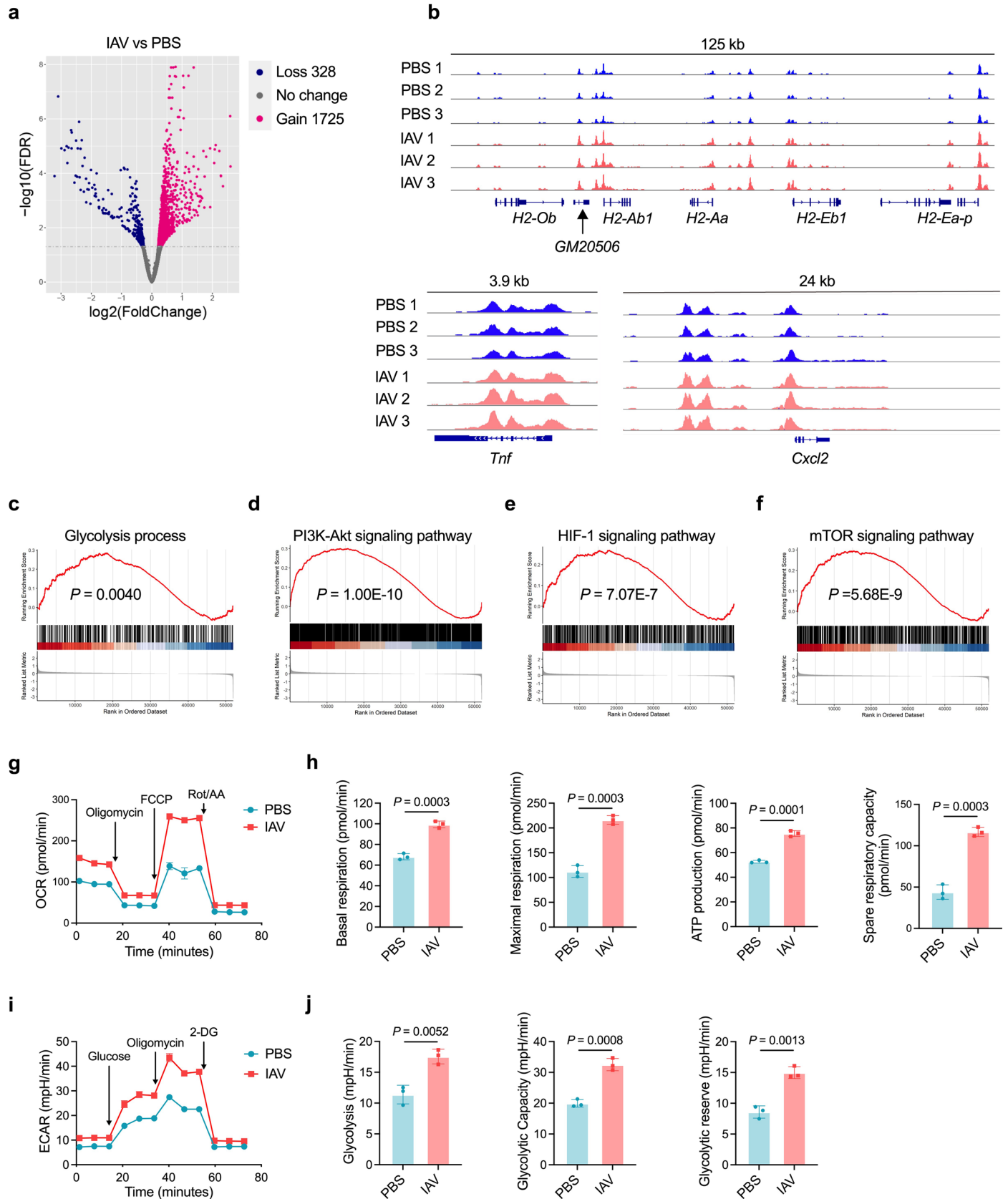
Extended Data Fig. 2 | Respiratory viral infections induce pulmonary anti-tumor immunity. (a) Quantification of B16 tumor burdens in PBS or IAV-infected mice. (b) Representative Masson's trichrome staining images of B16 tumor-bearing lungs from PBS or IAV-infected mice. Quantification of B16 cells based on RT-PCR (c) or flow cytometry (d) analysis in the lungs of PBS or IAV mice early post i.v. inoculation of B16-luc expressing GFP. (e) Macroscopy of lungs and (f) number of B16 tumor nodules on the lung surface in PBS and day 60 IAV-infected (IAV₆₀) mice. (g) Representative lung histopathology images and (h) percentage of lung area occupied by tumor lesions in mice shown in (e). (i) Macroscopy of lungs and (j) number of B16 tumor nodules on the lung surface in PBS and day 30 IAV- or AdV-infected mice. (k) Representative lung histopathology and (l) percentage of lung area occupied by tumor lesions in mice shown in (i). (m) Schema of subcutaneous (s.c.) B16 tumor model. (n) Kinetic changes in subcutaneous B16 tumor size at

the injection site. (o) Macroscopy and (p) weight of subcutaneous B16 tumors at endpoint. (q) Kinetics of subcutaneous tumor volume after inoculation of 4T1 cells in PBS or IAV-infected mice (* $p = 0.0336$). (r) Schema of bone marrow transplantation (BMT). (s) Percentage of donor-derived peripheral blood myeloid cells at 35 days post BMT. (t) average radiance of luciferin signals in the lung area and (u) number of B16 tumor nodules on the lung surface in mice shown in (r). Bar graphs are presented as mean \pm SD. Data are representatives of two independent experiments (n = 3 mice per group in a,c,d; n = 5 mice per group in b,f,h; n = 6 mice in PBS and IAV groups and n = 4 mice in AdV group in j,l; n = 4 mice per group in n,p,q; n = 6 mice per group in s,t,u). Two-tailed Student t test was performed for comparisons between two groups. One-way ANOVA followed by a Tukey test was performed to compare more than two groups.



Extended Data Fig. 3 | Depletion of T cells and AMs in lung tissues. (a,b) Absolute numbers of CD4⁺ T cells (a) and CD8⁺ T cells (b) in BAL and lung tissues in uninfected (PBS) or IAV-infected mice, or IAV-infected mice with i.p. injection of anti-CD4 and anti-CD8 depleting antibodies (IAV_{Tdepl}). (c) Relative numbers of AMs in BAL and lung tissues in PBS or IAV mice at 48 hours following i.t.

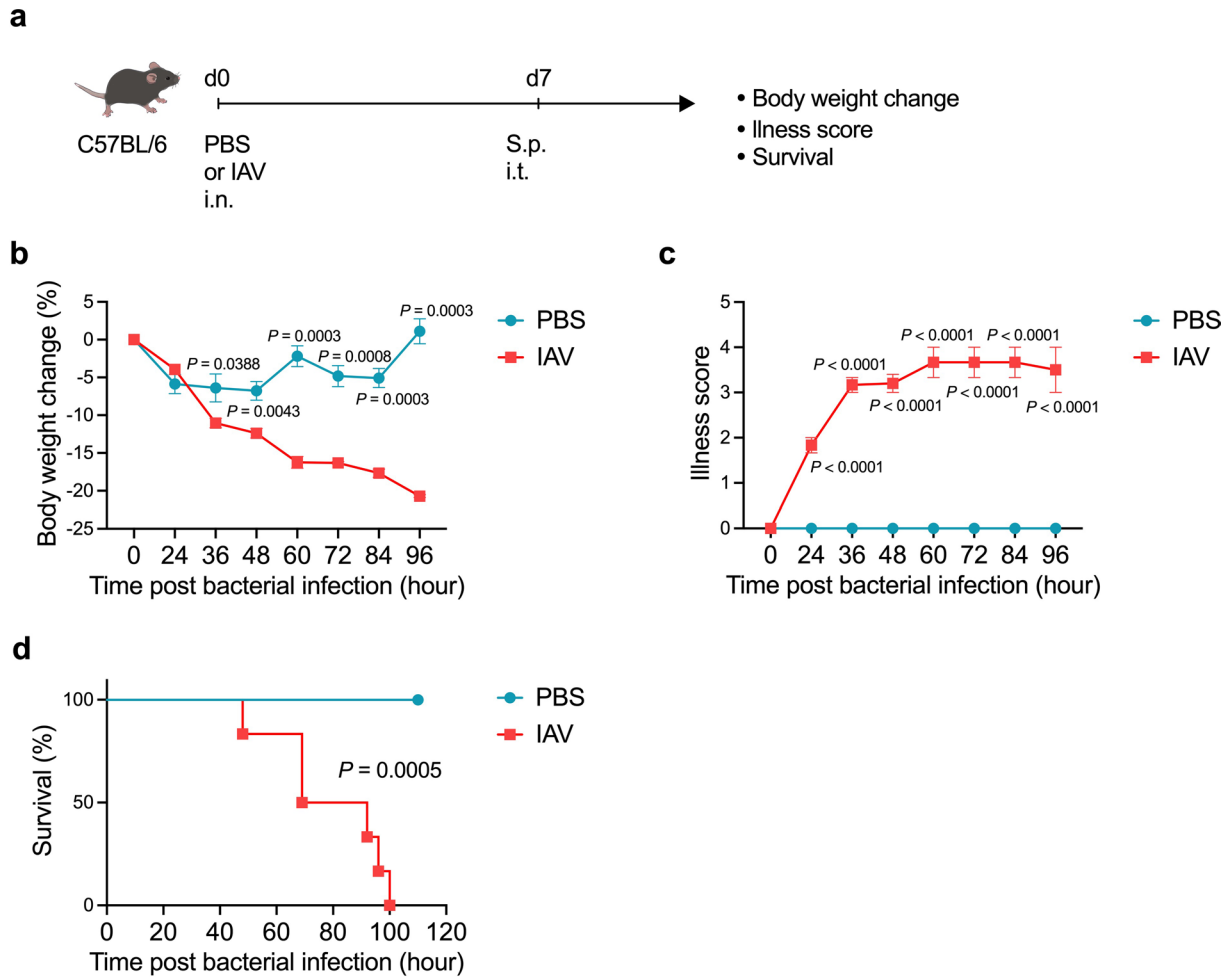
administration of either control liposomes (ctrl) or clodronate liposomes. Bar graphs are presented as mean ± SD. Data are representatives of two independent experiments with number of mice per group as indicated (n = 3 mice per group in a,b; n = 4 mice in PBS ctrl group, n = 3 mice in IAV ctrl group, and n = 2 mice per group in PBS clodronate and IAV clodronate groups in c).



Extended Data Fig. 4 | See next page for caption.

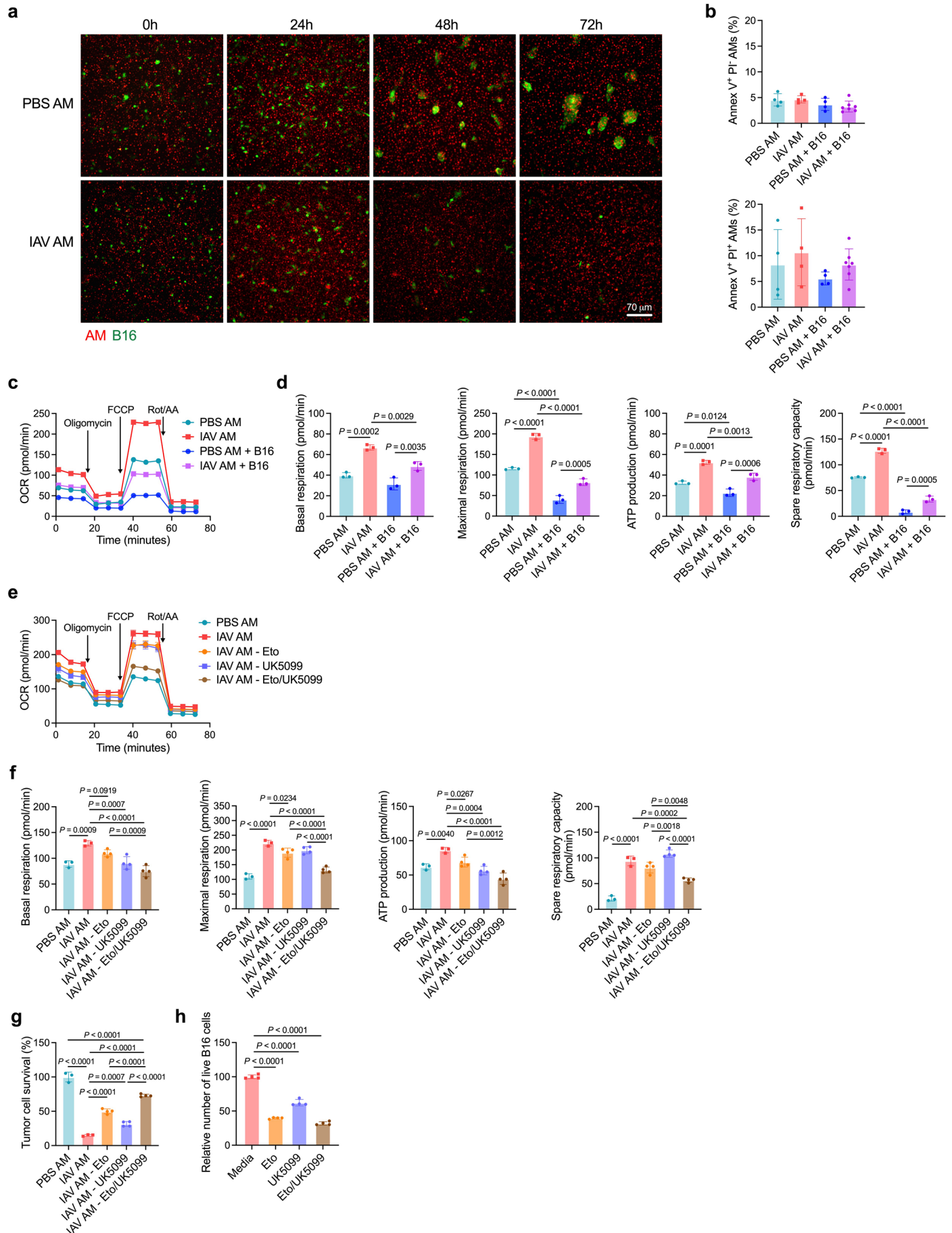
Extended Data Fig. 4 | IAV induces long-term epigenetic and metabolic changes in AMs. (a) ATAC-seq volcano plots showing genes with significant gain or loss (FDR < 0.05) of chromatin accessibility in AMs from day 30 IAV-infected mice as compared to those from uninfected (PBS) mice. (b) ATAC-seq signals for genes encoding MHC II (top), TNF (lower left), and CXCL2 (lower right) in AMs from IAV versus PBS mice. All tracks were group-autoscaled to enable comparison. (c-f) GSEA of ATAC-seq signals of genes related to glycolysis process (c), PI3K-Akt signaling pathway (d), HIF-1 signaling pathway (e), and mTOR signaling pathway (f), in AMs from IAV versus PBS mice. (g) Real-time oxygen

consumption rate (OCR) in PBS versus day 30 IAV AMs. (h) Basal respiration, maximal respiration, ATP production, and spare respiratory capacity in AMs shown in (g). (i) Real-time extracellular acidification rate (ECAR) in PBS versus day 30 IAV AMs. (j) Glycolysis, glycolytic capacity and glycolytic reserve in AMs shown in (i). Data are presented as mean \pm SD. Data in a-f are from one experiment with n = 3 mice per group. Data in g-j are representatives of three independent experiments with n = 3 replicate culture wells per group. Two-tailed Student t test was performed for comparisons between two groups.



Extended Data Fig. 5 | Acute phase of IAV infection is related to bacterial super-infection. (a) Schema of respiratory IAV infection followed by challenge with *Streptococcal pneumoniae* (S.p.) i.t. at 2×10^7 cfu per mouse on day 7 post viral infection. (b-d) Body weight change (b), illness score (c), and survival (d)

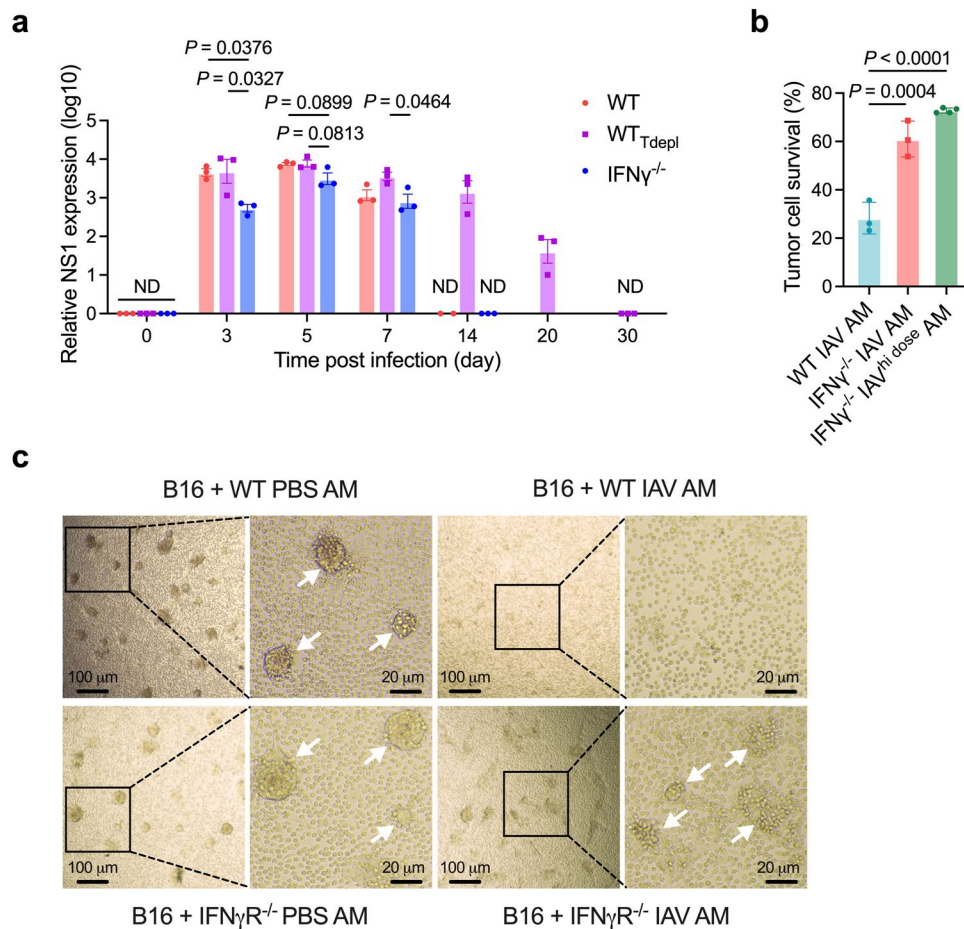
of mice after bacterial challenge. Data are presented as mean \pm SEM, and are representatives of two independent experiments with $n = 6$ mice per group. Two-tailed Student t test was performed for comparisons between two groups. Log-rank (Mantel-Cox) test was used for comparison of survival curves.



Extended Data Fig. 6 | See next page for caption.

Extended Data Fig. 6 | Anti-tumor trained AMs depend on enhanced mitochondrial oxidation. (a) Representative microscopic images on B16-GFP melanoma cells co-cultured with AMs isolated from PBS or day 30 IAV-infected mice and labeled with fluorescence dye. Cells were co-cultured for 72 hours at an AM:B16 (E:T) ratio of 20:1. (b) Flow cytometry analysis on Annexin V and PI in PBS or IAV AMs cultured alone or co-cultured with B16 melanoma cells for 48 hours. (c) Real-time oxygen consumption rate (OCR) in PBS versus IAV AMs cultured alone or co-cultured with B16 melanoma cells for 48 hours. (d) Basal respiration, maximal respiration, ATP production, and spare respiratory capacity in AMs shown in (c). (e) Real-time oxygen consumption rate (OCR) in PBS versus IAV AMs cultured *ex vivo* with Etomoxir (Eto) and/or UK5099. (f) Basal respiration, maximal respiration, ATP production, and spare respiratory

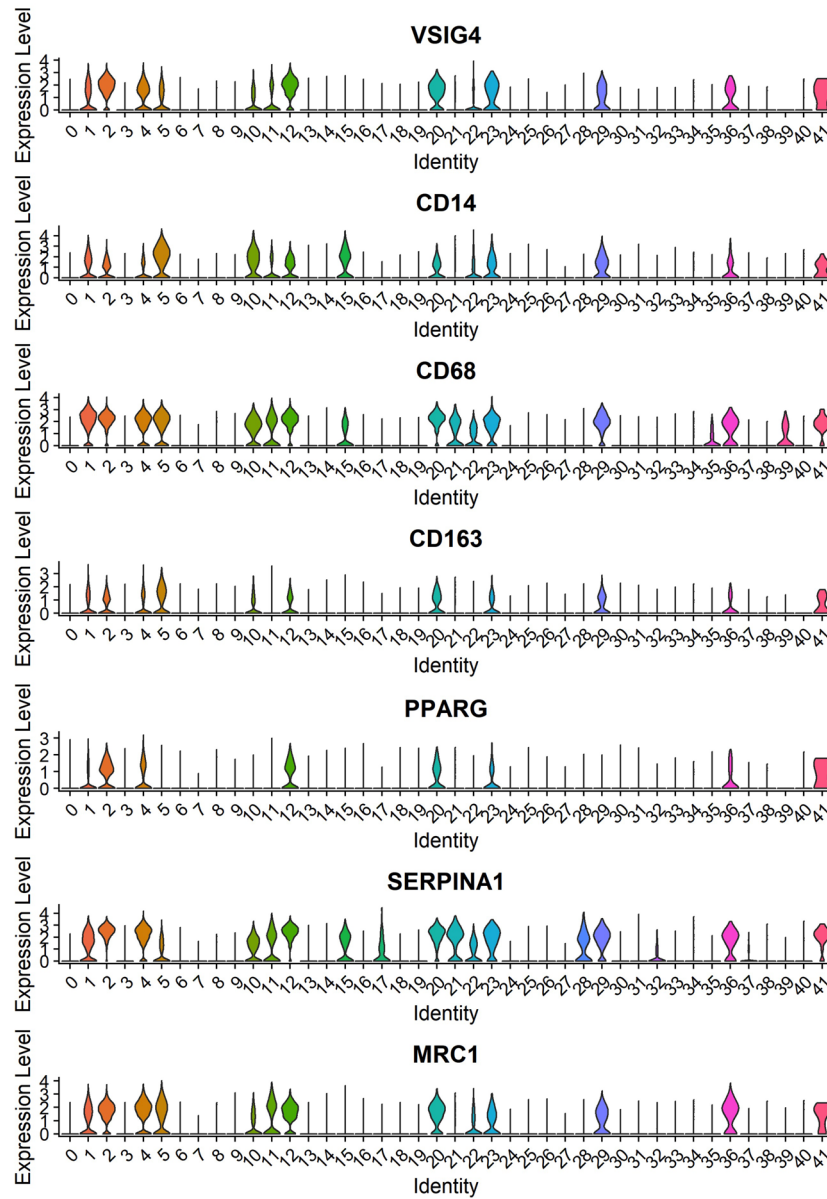
capacity in AMs shown in (e). (g) Survival of B16-luc melanoma cells co-cultured with PBS or IAV AMs for 72 hours in the presence of Etomoxir and/or UK5099. (h) Relative number of live B16-luc cells after culture alone for 72 hours in the presence of Etomoxir and/or UK5099. Data are presented as mean \pm SD and are representatives of three independent experiments with 3 replicate culture wells per group in a, or two independent experiments with the number of replicate culture wells per group as indicated in b-h (n = 7 wells in IAV AM + B16 group and n = 4 in other groups in b; n = 3 wells per group in c,d; n = 3 wells in PBS AM and IAV AM groups and n = 4 wells in other groups in e,f,g; n = 4 wells per group in h). One-way ANOVA followed by a Tukey test was performed to compare more than two groups.



Extended Data Fig. 8 | Generation of anti-tumor trained immunity in AMs depends on IFN γ . (a) Quantification of IAV based on RT-PCR of NS1 gene transcripts in the lungs of wild type (WT) mice with or without depletion of CD4⁺ and CD8⁺ T cells *in vivo*, or IFN γ knockout mice (IFN γ ^{-/-}). ND = not detected. (b) Survival of B16-luc melanoma cells co-cultured for 72 hours with AMs from day 30 IAV-infected WT or IFN γ ^{-/-} mice with either standard IAV infection dose (120 pfu per mouse) or high infection dose (360 pfu per mouse). (c) Representative microscopic images on B16 melanoma cells co-cultured with

AMs isolated from PBS or day 30 IAV-infected WT or IFN γ receptor knockout (IFN γ R^{-/-}) mice. Arrows indicate cellular clusters composed of B16 tumor cells and AMs. Bar graphs in a,b are presented as mean \pm SD. Data are representatives of two independent experiments with number of mice or replicate culture wells per group as indicated (n = 3 mice per group in a; n = 4 wells in IFN γ ^{-/-} IAV^{hi dose} AM group and n = 3 wells in other groups in b; n = 3 or 4 wells per group in c). One-way ANOVA followed by a Tukey test was performed to compare more than two groups.

a



Extended Data Fig. 9 | Identification of AM subpopulations in human NSCLC tissues. (a) scRNA-seq violin plots showing a total of forty-two cell populations in human NSCLC tumor tissues. Macrophages (clusters 1, 2, 4, 5, 10, 11, 12, 20, 23, 29, 36, 41) are characterized by co-expression of CD14, CD68, and MRC1, with or

without VSIG4 and CD163 expression, after exclusion of monocyte populations. AMs (clusters 1, 2, 4, 5, 10, 11, 12, 20) are defined as macrophages that express resident AM markers including PPARG and SERPINA1.

Reporting Summary

Nature Portfolio wishes to improve the reproducibility of the work that we publish. This form provides structure for consistency and transparency in reporting. For further information on Nature Portfolio policies, see our [Editorial Policies](#) and the [Editorial Policy Checklist](#).

Statistics

For all statistical analyses, confirm that the following items are present in the figure legend, table legend, main text, or Methods section.

n/a Confirmed

- The exact sample size (n) for each experimental group/condition, given as a discrete number and unit of measurement
- A statement on whether measurements were taken from distinct samples or whether the same sample was measured repeatedly
- The statistical test(s) used AND whether they are one- or two-sided
Only common tests should be described solely by name; describe more complex techniques in the Methods section.
- A description of all covariates tested
- A description of any assumptions or corrections, such as tests of normality and adjustment for multiple comparisons
- A full description of the statistical parameters including central tendency (e.g. means) or other basic estimates (e.g. regression coefficient) AND variation (e.g. standard deviation) or associated estimates of uncertainty (e.g. confidence intervals)
- For null hypothesis testing, the test statistic (e.g. F , t , r) with confidence intervals, effect sizes, degrees of freedom and P value noted
Give P values as exact values whenever suitable.
- For Bayesian analysis, information on the choice of priors and Markov chain Monte Carlo settings
- For hierarchical and complex designs, identification of the appropriate level for tests and full reporting of outcomes
- Estimates of effect sizes (e.g. Cohen's d , Pearson's r), indicating how they were calculated

Our web collection on [statistics for biologists](#) contains articles on many of the points above.

Software and code

Policy information about [availability of computer code](#)

Data collection

Flow cytometry: FACS Diva software version 8.0.1 (BD) ,Confocal microscopy: ZEN Black Imaging Software (ZEISS) , in vivo tumor imaging: Living image software

Data analysis

FastQC(v 0.11.5), Fastp (v0.19.11), Picard(v 1.111), BWA(v0.7.12-r1039), Samtools(v1.11), BedTools(v 2), MACS2(v2.1.2), DiffBind (v3.4) were used to generate ATACseq data. Data analysis was performed using R software (v 4.1.2), R-studio, and additional R packages: DESeq2(v 1.34.0), ggplot2(v3.3.6), pheatmap(v 1.0.12),clusterProfiler(v4.2.1), Seurat(v4.1.0), SingleR(v1.8.1), tidyverse(v1.3.1), patchwork(v1.1.1), DiffBind(v3.4), ChIPseeker(v1.30.3), corrplot(v0.92), ggridges(v0.5.3), enrichplot(v1.14.1). Mouse assembly version mm10/NCBI m38 was used for sequence alignments with hisat2 version2.0.5.
Flow cytometry data were analyzed using FlowJo (v10.7.1). Data was visualized using Graphpad (V9, Prism software).
OCR and ECAR data on AM metabolism were analyzed using Wave Desktop software (v2.6).

For manuscripts utilizing custom algorithms or software that are central to the research but not yet described in published literature, software must be made available to editors and reviewers. We strongly encourage code deposition in a community repository (e.g. GitHub). See the Nature Portfolio [guidelines for submitting code & software](#) for further information.

Data

Policy information about [availability of data](#)

All manuscripts must include a [data availability statement](#). This statement should provide the following information, where applicable:

- Accession codes, unique identifiers, or web links for publicly available datasets
- A description of any restrictions on data availability
- For clinical datasets or third party data, please ensure that the statement adheres to our [policy](#)

RNA-seq data and ATAC-seq data are deposited in the NCBI's GEO under accession code GSE222150 (<https://www.ncbi.nlm.nih.gov/geo/query/acc.cgi?acc=GSE222150>). Human scRNA-seq data were previously published (Cancer Cell. 2021 Dec 13;39(12):1594-1609.e12. doi: 10.1016/j.ccell.2021.10.009.) and can be accessed under accession code GSE154826 (<https://www.ncbi.nlm.nih.gov/geo/query/acc.cgi?acc=GSE154826>).

Field-specific reporting

Please select the one below that is the best fit for your research. If you are not sure, read the appropriate sections before making your selection.

- Life sciences Behavioural & social sciences Ecological, evolutionary & environmental sciences

For a reference copy of the document with all sections, see [nature.com/documents/nr-reporting-summary-flat.pdf](https://www.nature.com/documents/nr-reporting-summary-flat.pdf)

Life sciences study design

All studies must disclose on these points even when the disclosure is negative.

Sample size	No statistical methods were used to pre-determine sample sizes, but our sample sizes are similar to those reported in previous publications (Jeyanathan, M. et al. Nat Immunol 23, 1687–1702 (2022); Yao, Y. et al. Cell 175, 1634–1650.e17 (2018).). Data distribution was assumed to be normal, but this was not formally tested.
Data exclusions	No data points were excluded from analysis.
Replication	Experiments were performed independently for two to three times, except that ATAC-seq experiments were performed once, as indicated in figure legends. And each experiment gave similar results.
Randomization	Mice of comparable age and body weight were randomly assigned to groups prior to the initiation of experiment.
Blinding	Data collection and analysis were not performed blind to the conditions of the experiments.

Reporting for specific materials, systems and methods

We require information from authors about some types of materials, experimental systems and methods used in many studies. Here, indicate whether each material, system or method listed is relevant to your study. If you are not sure if a list item applies to your research, read the appropriate section before selecting a response.

Materials & experimental systems

n/a	Involved in the study
<input type="checkbox"/>	<input checked="" type="checkbox"/> Antibodies
<input type="checkbox"/>	<input checked="" type="checkbox"/> Eukaryotic cell lines
<input checked="" type="checkbox"/>	<input type="checkbox"/> Palaeontology and archaeology
<input type="checkbox"/>	<input checked="" type="checkbox"/> Animals and other organisms
<input checked="" type="checkbox"/>	<input type="checkbox"/> Human research participants
<input checked="" type="checkbox"/>	<input type="checkbox"/> Clinical data
<input checked="" type="checkbox"/>	<input type="checkbox"/> Dual use research of concern

Methods

n/a	Involved in the study
<input checked="" type="checkbox"/>	<input type="checkbox"/> ChIP-seq
<input type="checkbox"/>	<input checked="" type="checkbox"/> Flow cytometry
<input checked="" type="checkbox"/>	<input type="checkbox"/> MRI-based neuroimaging

Antibodies

Antibodies used

The following antibodies were used: Antibody / Company / Dilution used / Catalogue number

The following antibodies were used for flow cytometry:
 CD16/CD32 (clone 2.4G2) BD Biosciences 1:200 Cat# 553141
 CD45 APC-Cy7 (clone 30-F11) BD Biosciences 1:400 Cat# 557659
 CD45.1 APC-Cy7 (clone A20) BD Biosciences 1:200 Cat# 560579
 CD45.2 PerCP-Cy5.5 (clone 104) Biolegend 1:200 Cat# 109828
 CD11b PE-Cy7 (clone M1/70) BD Biosciences 1:400 Cat# 552850

CD11c APC (clone N418) Biolegend 1:200 Cat#117310
 I-A/I-E Alexa Flour 700 (clone M5/114.15.2) Biolegend 1:200 Cat# 107622
 CD3-V450 (clone 17A2) BD Biosciences 1:200 Cat# 561389
 Ly-6C BV711(clone HK1.4) Biolegend 1:500 Cat# 128037
 Ly6G-BV650 (clone 1A8) Biolegend 1:500 Cat# 127641
 CD24-BV605 (clone M1/69) Biolegend 1:500 Cat# 101827
 CD64-PE (clone X54-5/7.1) BD Biosciences 1:200 Cat# 558455
 Siglec-F PE-CF594 (clone E50-2440) BD Biosciences 1:500 Cat# 562757
 CD4 PE-Cy7 (clone RM4-5) BD Biosciences 1:200 Cat# 552775
 CD8-APC-Cy7 (clone 53-6.7) BD Bioscience 1:400 Cat# 557654
 BrdU-APC mAb (clone B44) BD Biosciences 1:50 Cat# 51-23619L
 CD45.1 FITC (clone A20) Biolegend 1:200 Cat# 110705
 CD11b BV605(clone M1/70) Biolegend 1:500 Cat# 101237
 CD11c PE-Cy7(clone N418) Biolegend 1:200 Cat# 117317
 IFN- γ APC(clone XMG1.2) Biolegend 1:200 Cat# 505810
 TCRgd FITC(clone GL3) Biolegend 1:200 Cat# 118105
 CD49b PE(clone DX5) BD Bioscience 1:400 Cat# 561066
 CD3 PE-CF594(clone 17A2) Biolegend 1:400 Cat# 100245
 CD45R V450(clone RA3-6B2) BD Bioscience 1:200 Cat# 560473
 TCRab PE-Cy7(clone H57-597) Biolegend 1:200 Cat# 109222
 F4/80 PE-Cy7(clone BM8) Biolegend 1:200 Cat# 123109
 Fc ϵ R1a PE-Cy7(clone MAR-1) eBioscience 1:200 Cat# 25-5898-80
 Gata3 PE(clone TWAJ) eBioscience 1:200 Cat# 12-9966-41
 lin(anti-mouse CD3 ϵ , clone 145-2C11; anti-mouse Ly-6G/Ly-6C, clone RB6-8C5; anti-mouse CD11b, clone M1/70; anti-mouse CD45R/B220, clone RA3-6B2; anti-mouse TER-119/Erythroid cells, clone Ter-119) Biolegend 1:200 Cat#133307
 Streptavidin Percp-Cy5.5 eBioscience 1:200 Cat# 45-4317-80
 The following primary antibodies were used for immunofluorescence (IF) staining:
 CD3(clone SP7) Abcam 1:100 Cat# ab16669
 Siglec-f(clone 1RNM44N) Thermo Fisher 1:200 Cat# 14-1702-82
 CD11c(clone N418) Biolegend 1:100 Cat# 117314
 The following secondary antibodies were used for immunofluorescence (IF) staining:
 Goat anti-rat IgG (H+L) AF488 Thermo Fisher 1:500 Cat# A48262
 Goat anti-mouse IgG (H+L) AF488 Thermo Fisher 1:500 Cat# A-11001
 Donkey anti-Rabbit IgG (H+L) AF647 Thermo Fisher 1:500 Cat# A32795TR
 Donkey anti-mouse IgG (H+L) AF594 Jackson ImmunoResearch 1:500 Cat# 146552

Other antibodies used in the manuscript:
 CD47(clone Miap301) Biolegend 10 μ g/ml Cat# 127517
 CD4 antibody (clone GK1.5) BioXCell Cat# BE0003-1 diluted and used as indicated in the Methods section in the manuscript
 CD8 antibody (clone 2.43) BioXCell Cat# BE0061 diluted and used as indicated in the Methods section in the manuscript
 NK1.1 antibody(clone PK136) made in house diluted and used as indicated in the Methods section in the manuscript

Validation

The following antibodies were used: Antibody / Company / Dilution used / Cat# / Validation
 CD16/CD32 (clone 2.4G2) BD Biosciences 1:200 Cat# 553141 RRID:AB_394656
 CD45 APC-Cy7 (clone 30-F11) BD Biosciences 1:400 Cat# 557659 RRID:AB_396774
 CD45.1 APC-Cy7 (clone A20) BD Biosciences 1:200 Cat# 560579 RRID:AB_1727487
 CD45.2 PerCP-Cy5.5 (clone 104) Biolegend 1:200 Cat# 109828 RRID:AB_893350
 CD11b PE-Cy7 (clone M1/70) BD Biosciences 1:400 Cat# 552850 RRID:AB_394491
 CD11c APC (clone N418) Biolegend 1:200 Cat#117310 RRID:AB_313779
 I-A/I-E Alexa Flour 700 (clone M5/114.15.2) Biolegend 1:200 Cat# 107622 RRID:AB_493727
 CD3-V450 (clone 17A2) BD Biosciences 1:200 Cat# 561389 RRID:AB_10679120
 Ly-6C BV711(clone HK1.4) Biolegend 1:500 Cat# 128037 RRID:AB_2562630
 Ly6G-BV650 (clone 1A8) Biolegend 1:500 Cat# 127641 RRID:AB_2565881
 CD24-BV605 (clone M1/69) Biolegend 1:500 Cat# 101827 RRID:AB_2563464
 CD64-PE (clone X54-5/7.1) BD Biosciences 1:200 Cat# 558455 RRID:AB_647241
 Siglec-F PE-CF594 (clone E50-2440) BD Biosciences 1:500 Cat# 562757 RRID:AB_2687994
 CD4 PE-Cy7 (clone RM4-5) BD Biosciences 1:200 Cat# 552775 RRID:AB_394461
 CD8-APC-Cy7 (clone 53-6.7) BD Bioscience 1:400 Cat# 557654 RRID:AB_396769
 BrdU-APC mAb (clone B44) BD Biosciences 1:50 Cat# 552598 RRID:AB_2861367
 CD45.1 FITC (clone A20) Biolegend 1:200 Cat# 110705 RRID:AB_313494
 CD11b BV605(clone M1/70) Biolegend 1:500 Cat# 101237 RRID:AB_11126744
 CD11c PE-Cy7(clone N418) Biolegend 1:200 Cat# 117317 RRID:AB_493569
 IFN- γ APC(clone XMG1.2) Biolegend 1:200 Cat# 505810 RRID:AB_315404
 TCRgd FITC(clone GL3) Biolegend 1:200 Cat# 118105 RRID:AB_313829
 CD49b PE(clone DX5) BD Bioscience 1:400 Cat# 561066 RRID:AB_10563616
 CD3 PE-CF594(clone 17A2) Biolegend 1:400 Cat# 100245 RRID:AB_2565882
 CD45R V450(clone RA3-6B2) BD Bioscience 1:200 Cat# 560473 RRID:AB_1645277
 TCRab PE-Cy7(clone H57-597) Biolegend 1:200 Cat# 109222 RRID:AB_893625
 F4/80 PE-Cy7(clone BM8) Biolegend 1:200 Cat# 123109 RRID:AB_893498
 Fc ϵ R1a PE-Cy7(clone MAR-1) Thermo Fisher Scientific 1:200 Cat# 25-5898-80 RRID:AB_2573492
 Gata3 PE(clone TWAJ) Thermo Fisher Scientific 1:200 Cat# 12-9966-41 RRID:AB_1963601
 lin(anti-mouse CD3 ϵ , clone 145-2C11; anti-mouse Ly-6G/Ly-6C, clone RB6-8C5; anti-mouse CD11b, clone M1/70; anti-mouse CD45R/B220, clone RA3-6B2; anti-mouse TER-119/Erythroid cells, clone Ter-119) Biolegend 1:200 Cat#133307 RRID:AB_11124348
 Streptavidin Percp-Cy5.5 Thermo Fisher Scientific 1:200 Cat# 45-4317-80 RRID:AB_10260035
 CD3(SP7) Abcam 1:100 Cat# ab16669 RRID:AB_443425

Siglec-f(clone 1RNM44N) Thermo Fisher 1:200 Cat# 14-1702-82 RRID:AB_2572866
 CD11c(clone N418) Biolegend 1:100 Cat# 117314 RRID:AB_492850
 CD47(clone Miap301) Biolegend 10 µg/ml Cat# 127517 RRID:AB_2571996
 CD4 antibody (clone GK1.5) BioXCell Cat# BE0003-1 diluted and used as indicated in the Methods section in the manuscript RRID:AB_1107636
 CD8 antibody (clone 2.43) BioXCell Cat# BE0061 diluted and used as indicated in the Methods section in the manuscript RRID:AB_1125541
 NK1.1 antibody (clone PK136) Flow cytometry-Quality tested
 Goat anti-rat IgG (H+L) AF488 Thermo Fisher 1:500 Cat# A48262 RRID:AB_2896330
 Goat anti-mouse IgG (H+L) AF488 Thermo Fisher 1:500 Cat# A-11001 RRID:AB_2534069
 Donkey anti-Rabbit IgG (H+L) AF647 Thermo Fisher 1:500 Cat# A32795TR RRID:AB_2866496
 Donkey anti-mouse IgG (H+L) AF594 Jackson ImmunoResearch 1:500 Cat# 146552 Flow cytometry - Quality tested

Eukaryotic cell lines

Policy information about [cell lines](#)

Cell line source(s)	B16F10 (B16; ATCC CRL-6475); GFP-expressing B16F10 cell line (B16-GFP) was generated from luciferase-expressing B16F10 (B16-luc; ATCC CRL-6475-LUC2) by transduction with lentiviral vector encoding GFP gene under EF-1 alpha promoter. 4T1 (ATCC CRL-2539).
Authentication	Cells were functionally authenticated: B16 cells and 4T1 cells were injected intravenously or subcutaneously into mice and tumor progression in the lung or at subcutaneous injection sites at different time points was followed.
Mycoplasma contamination	All cell lines tested negative for mycoplasma.
Commonly misidentified lines (See ICLAC register)	No commonly misidentified cell lines were used in this study.

Animals and other organisms

Policy information about [studies involving animals](#); [ARRIVE guidelines](#) recommended for reporting animal research

Laboratory animals	Wild-type female C57BL/6 mice and BALB/c mice were purchased from Slac Laboratory Animals (Shanghai, China). CD45.1 congenic mice on a C57BL/6 background (B6.SJL-Ptprca Pepcb/BoyJ) were originally from the Jackson Laboratory (Bar Harbor, ME). Interferon-gamma (IFN-γ) knockout mice on a C57BL/6 background (B6.129S7-Iflngtm1Ts/J) were originally from the Jackson Laboratory (Bar Harbor, ME). CCR2 knockout mice on a C57BL/6 background (B6.129S4-Ccr2tm1lfc/J) were originally from the Jackson Laboratory (Bar Harbor, ME). IFN-γ receptor knockout mice on a C57BL/6 background were generated by GemPharmatech (Nanjing, China). Mice were housed in specific pathogen-free facility with ad libitum access to food and water, 12hrs light cycle, 50-60% humidity and at 20-25°C room temperature at Zhejiang University Laboratory Animal Center. Age matched mice and housed in the same room were used in each experiment. Female mice of 6-8 weeks of age were used in all experiments.
Wild animals	No wild animals were used in this study.
Field-collected samples	This study did not use samples collected from the field.
Ethics oversight	All mouse experiments were carried out in accordance with the guidelines from the Animal Research and Ethics Boards of Zhejiang University.

Note that full information on the approval of the study protocol must also be provided in the manuscript.

Flow Cytometry

Plots

Confirm that:

- The axis labels state the marker and fluorochrome used (e.g. CD4-FITC).
- The axis scales are clearly visible. Include numbers along axes only for bottom left plot of group (a 'group' is an analysis of identical markers).
- All plots are contour plots with outliers or pseudocolor plots.
- A numerical value for number of cells or percentage (with statistics) is provided.

Methodology

Sample preparation	Mice were anesthetized with isoflurane and peripheral blood was exhaustively collected from the abdominal vein. Following exhaustive bronchoalveolar lavage with PBS, lung lobes were harvested, cut into small pieces, and digested in collagenase type I for 1 hour at 37 °C in a shaker incubator. Lung single-cell suspension was obtained by crushing the digested lung tissues through a 100 µm basket filter. Following erythrocyte lysis of peripheral blood and lung cells by incubation with red blood cell lysing buffer, cells were washed with PBS and resuspended in PBS for flow cytometry staining and analysis.
--------------------	--

Instrument	BD LSRFortessa (BD Bioscience)
Software	Data collection: BDFACSDiva (v8.0.1) software Data analysis: Flow cytometric data was analysed using Flowjo (v10.7.1)
Cell population abundance	Cell populations were sorted at >95% purity, determined by flow cytometric analysis of post-sort samples.
Gating strategy	Gating strategy is exemplified in the extended data figures and was reported in our previous publication (Yao, Y. et al. Cell 175, 1634-1650.e17 (2018)). Briefly, all cell events on FSC/SSC plot are included as the starting cell population, followed by excluding debris, dead cells and non-immune cells based on differential staining of CD45 surface marker and viability dye. Doublets are excluded based on SSC-A/SSC-H plot. Live leukocyte singlets are used to define immune cell subsets based on characteristic surface markers. For each marker, "positive" and "negative" cell populations are defined based on FMO.

Tick this box to confirm that a figure exemplifying the gating strategy is provided in the Supplementary Information.